Rock Mechanics and Rock Engineering
https://doi.org/10.1007/s00603-026-05478-z

ORIGINAL PAPER

Linking Ultrasonic Velocity and Microseismic Monitoring During Laboratory Triaxial Deformation of Reservoir Sandstones from a North Sea CO_2 Storage Site

Debanjan Chandra[1,2] · Milad Naderloo[2] · Lars Grande[3] · Luke Griffiths[3] · Auke Barnhoorn[2]

Received: 2 July 2025 / Accepted: 18 March 2026

Abstract

Subsurface fluid injections cause rapid thermal and stress changes near wells, potentially compromising reservoir integrity. Effective monitoring and mitigation strategies are essential to ensure safe operations. This study investigates highly porous North Sea sandstones under low confining pressures (1 and 3 MPa), replicating near-wellbore stress conditions for a saline aquifer during CO_2 injection. Using triaxial deformation experiments, we analyze the evolution of ultrasonic velocities, amplitudes, and acoustic emission (AE) signals to track deformation processes. Our results demonstrate that combined ultrasonic and AE monitoring effectively captures and forecasts the transition from elastic to inelastic deformation. An empirical relationship is proposed demonstrating a proof-of-concept correlation between microseismic event counts and ultrasonic velocity during irreversible deformation, which, upon calibration can be used for site-specific stress state monitoring. Higher confinement leads to increased AE activity due to intensified grain crushing and interparticle locking. At constant confinement, more porous samples also show greater AE activity, indicating enhanced damage accumulation. Spectral analysis reveals increased attenuation at higher confining pressures and a shift toward lower frequencies near failure, suggesting dominant shear deformation. Notably, deformation patterns vary with confinement: low confinement induces frictional slip and distinct failure planes, while high confinement promotes distributed damage and porosity reduction through grain crushing. This results in a non-linear failure envelope shaped by the dominant deformation mechanisms. These findings enhance our understanding of pore fluid-induced changes in reservoir rocks and offer new strategies for monitoring CO_2 storage and other subsurface injection operations, especially in heterogeneous, porous formations under varying stress regimes.

Highlights

- Combined ultrasonic and microseismic monitoring tracks stress buildup and failure in reservoir sandstones.
- A clear link is shown between the decrease of wave velocity and increasing microseismic events during progressive deformation.
- High porosity and confinement promote grain crushing and wider damage zone, increasing microseismicity.
- An empirical relationship connects ultrasonic velocity and microseismicity during irreversible deformation.
- Findings help predict and monitor safe stress limits for CO_2 storage and other fluid injection operations.

Keywords Acoustic emission · Ultrasonic velocity · Subsurface monitoring · Traffic light scenario · CO_2 storage

✉ Debanjan Chandra
debanjan.chandra@ntnu.no

[1] Department of Geosciences (IGV), Norwegian University of Science and Technology (NTNU), S. P. Andersens veg 15a, 7031 Trondheim, Norway

[2] Department of Geoscience and Engineering, Delft University of Technology, Stevinweg 1, 2628 CN Delft, The Netherlands

[3] Norwegian Geotechnical Institute (NGI), 0806 Oslo, Norway

Published online: 09 April 2026

1 Introduction

Stress-induced rock deformation is one of the major risks in subsurface CO_2 and energy storage applications (Ramesh Kumar et al. 2023). Injection of CO_2 in depleted hydrocarbon reservoirs and saline aquifers alters the effective stresses from changes in pore pressure and temperature, which may cause harmless elastic expansion of the reservoir and potential uplift (Rutqvist et al. 2010; Teatini et al. 2011; Li et al. 2015), but also unwanted fault reactivation, induced seismicity, or irreversible deformation of the reservoir rock. Stress changes from both pore pressure increase and cooling due to injection of CO_2 need to be accounted for when scoping a storage site. Reduction in effective stress from elevated pore pressure is linked to the injection pressure and limited by the capacity of the sealing formation. Injection of non-isothermal fluids like CO_2, depending on the reservoir depth and thermal gradient between injected CO_2 and reservoir formation, can also lead to rapid cooling of the formation near the wellbore which may cause a reduction in total and effective horizontal stresses due to thermo-elasticity (Fjær et al. 2008). For some cases of deep stiff reservoirs with a high difference between injected fluid and reservoir temperature, this can lead to large reduction in effective horizontal stresses and increased shear stresses with a potential for micromechanical damage and failure (Grande et al. 2024). Therefore, understanding the reservoir deformation behavior at low effective stresses is important to mitigate risks for containment.

Norway has been at the forefront of subsurface CO_2 storage, with the success of the Sleipner project motivating many other countries to venture into subsurface CO_2 storage programs (Kongsjorden et al. 1998; Holloway et al. 2000). The Northern Lights CCS project, situated in offshore Norway, is the world's first cross-border CO_2 transport and storage facility with a potential injection rate of 1.5 million tons of CO_2 per year. CO_2 injection into saline aquifers must ensure successful containment over a long period, and several studies have focused on the characterization of in situ stress (Thompson et al. 2022), thermal stress changes in caprock (Thompson et al. 2021), and reservoir (Grande et al. 2024) and the geomechanical properties of the reservoir and caprock (Griffith et al. 2025; Grande et al. 2024). In a deep saline aquifer setting such as 2.6 km deep Aurora reservoir in the Northern Lights project, it has been found that both pore pressure and temperature in combination may contribute to a low effective stress in the reservoir sandstone formation near the wellbore due to a large cooling of 80 °C (Thompson et al. 2021; Grande et al. 2024). Generally, elevated pore pressure is first expected to develop locally and transiently, particularly in the near-wellbore region and in zones experiencing rapid pore pressure increase during ramp-up phases of injection, or during pressure transients associated with operational changes. However, maximum injection pressure is also limited by the operational margins not to exceed the capacity of the sealing formation. Additionally, reduced effective horizontal stress from cooling may lead the stress path into a damage and failure regime in the low effective stress range. It is therefore relevant to study the details of the failure criteria in the low effective stress range. Laboratory tests conducted at low confining stress (low effective stress) therefore provide a mechanistic analog for these stress states, allowing deformation processes that may not be activated at higher confining stress to be directly investigated under controlled conditions. From a mechanical perspective, deformation at low confining stress is dominated by brittle processes such as frictional sliding, tensile or mixed-mode cracking, and strain localization along discrete failure planes, with limited grain crushing and strong sensitivity to small changes in effective stress (Wong et al. 1997; Baud et al. 2000; Fortin et al. 2009). In contrast, higher confinement suppresses tensile cracking and promotes distributed cataclastic deformation, pore collapse, and grain crushing, resulting in more diffuse damage zones, reduced stress drops, and a transition toward ductile behavior (Wong et al. 1997; Baud et al. 2000; Fossen et al. 2007; Zhang et al. 2015). Consequently, low-confinement experiments are particularly suited to isolating deformation mechanisms relevant to near-wellbore stress state, where localized brittle damage and early irreversible deformation may occur well before a potential larger-scale failure in reservoir or caprock is expected. If the damage process is well understood and captured by monitoring, such damage may be used to characterize the state of stress and deformation in the reservoir for safe injection.

However, direct monitoring of stress conditions in the subsurface during and following CO_2 injection remains challenging. Techniques including time lapse 3D seismic, gravity, and electromagnetic surveys, as well as microseismic array, tiltmeter, and InSAR monitoring, have been commonly employed in many CO_2 storage projects worldwide (Eiken et al. 2011; Ringrose et al. 2013; Will et al. 2014; Goertz-Allmann et al. 2014; Furre et al. 2017; Lüth and Liebscher 2017). A poor cost–benefit ratio of the chosen monitoring technique can jeopardize the economic viability of the project (Mathieson et al. 2011). Recent works on improvement of borehole and cross-well seismic monitoring (Chalaturnyk et al. 2006; Lawton et al. 2006; Daley et al. 2007, 2008; White et al. 2021; Pevzner et al. 2021), supported by laboratory-scale experiments to determine stress-dependent changes in elastic properties (Barnhoorn et al. 2018; Agofack et al. 2018; Zotz-Wilson et al. 2019; Veltmeijer et al. 2023, 2024; Holt et al. 2023; Lozovyi et al. 2024; Chandra and Barnhoorn 2025; Chandra et al. 2025), have established active acoustic surveys as a cheaper and effective alternative for monitoring, especially for near-wellbore stress alterations. Passive microseismic monitoring, on the other hand, is extensively used for reservoirs with high risk of fault reactivation (Goertz-Allmann et al. 2014; Bauer et al. 2016). Fracture formation and small-scale displacement along a fault plane within the reservoir complex can be picked up by the acoustic sensors, allowing source location and providing insights into the underlying deformation mechanics (Sellers et al. 2003; Naderloo et al. 2023; Heimisson et al. 2024). At the laboratory scale, experiments on stress-induced ultrasonic acoustic emission (AE) measurement provide insights into the impact of pore fluid, porosity, grain size, and confinement on inelastic deformation of sandstones (Biot 1962; Siggins and Dewhurst 2003; Mayr et al. 2011; Komijani et al. 2019; Baizhanov et al. 2019; Yang et al. 2020). From a monitoring perspective, although active seismic velocity or attenuation measurements indicate deformation in a rock mass, it fails to locate the zones of weakness or the type of deformation event (tensile or shear). These insights are helpful for operators to employ targeted remediation plans. Microseismic monitoring can provide direct information of stress state, during inelastic deformation, provided there is a good array of sensors, which can locate the events (Vavryčuk 2001; Griffiths et al. 2019), also with an assumption that induced seismicity can be segregated from natural ones. However, limited information can be extracted during elastic deformation, where the number of detectable microseismic events is too low. Therefore, a combination of both active seismic and microseismic monitoring has a strong scope for robust monitoring of subsurface CO_2 injection.

Experiments have shown a strong relationship between porosity, confining stresses, and acoustic emission behavior in sandstones. For low-porosity sandstones, the deformation mechanism is primarily shear localization, whereas, for high-porosity sandstones, an increase in the number of microseismic events is caused by grain crushing, cataclastic compaction, and pore collapse (Fortin et al. 2009). Therefore, with increase in porosity, sandstones produce an order of magnitude more cumulative events during inelastic deformation. An increase in confinement on the other hand promotes ductile deformation, causing microseismic events to be temporally spread out with suppressed magnitudes (Yang et al. 2018; Huang et al. 2021). An increase in confinement also transforms nature of damage from predominantly tension type to shear type and produces less diffused and smoother crack surfaces post-failure (Huang et al. 2021).

This study investigates the deformation behavior of porous reservoir sandstones (23–32% porosity) belonging to a saline aquifer located offshore Norway to assess their mechanical properties at low confinements (low effective horizontal stress), compare with their respective failure behavior at higher confinement using experimental data from Grande et al. (2024), and provide indications on how active and passive sonic monitoring could be employed to quantify and forecast irreversible deformation in the reservoir. Note that the direct impact of temperature on micromechanical processes and related effects on velocity and AE is not tested in this study and not discussed here. This is avoided due to the practical complexity of combining temperature change and thermal stress paths into such experiments. However, we use the expected effective stresses induced by a combination of pore pressure increase and cooling in the field as the low effective stress boundary condition for our laboratory experiments.

2 Methodology

2.1 Sample Description

The core samples used in this work are sourced from different depths of the Eos 31/5–7 exploration well (https://factpages.sodir.no/en/wellbore/pageview/CO2storage/8951) in the Aurora CO_2 injection site in North Sea, offshore Norway. The samples used for this study belong to the Johansen and overlying Cook Formations, which are identified as the primary and secondary CO_2 storage formations, respectively, with the overlying Drake Formation being the primary seal (Halland et al. 2011; Andfossen et al. 2012; Meneguolo et al. 2020, 2022). The Johansen Formation, part of the Early Jurassic Dunlin Group, is a high-energy shallow-marine sandstone sequence located in the eastern and central Horda Platform of the northern North Sea, gradually pinching out westward (Meneguolo et al. 2022). The Johansen Formation serves as the primary CO_2 storage target for the Northern Lights project (https://norlights.com/), owing to its favorable lateral connectivity, high porosity, and permeability, which facilitate efficient plume redistribution. The Cook Formation, also part of the Dunlin Group, extends over a larger area than the Johansen Formation, reaching further north, west, and south across the Horda Platform. The lower part contains high-angle cross-stratified sandstones with well-sorted grains, while the upper portion shows increased tidal influence, marked by fining-upward sequences and thinner foreset beds (Meneguolo et al. 2022).

The geomechanical properties, strength, and stiffness from laboratory tests and logs are described previously for the Johansen and Cook formation (Grande et al. 2024; Griffiths et al. 2025) and for the caprock (Thompson et al. 2021, 2024; Griffiths et al. 2025). The specimens received (Table 1) were saturated with in situ reservoir brine (salinity similar to 8% NaCl solution), pre-cut, and with a 1″ diameter and 2″ length for the triaxial tests. Samples were not subjected to any treatment before testing. We received

2 plugs each of seal peels (SP), SP2 and SP4 and one from SP3, which were extracted from a larger 12.25″ diameter core. The plugs of the three SPs were drilled out in a previous testing campaign at NGI and triaxial tests performed on the same plugs at higher confinement have been reported in various papers (Grande et al. 2024; Griffiths et al. 2025). Data are available on the CO_2 Datashare platform (Northern Lights JV 2023).

Porosity values derived from X-ray CT images (Porosity*) represent only resolvable pore space at the chosen voxel resolution (15 μm) and therefore exclude pores and pore throats smaller than approximately 30 μm (detailed in Sect. 2.3). As a result, CT-derived porosity significantly underestimates total porosity compared to bulk measurements reported in the literature (Porosity#; Griffiths et al. 2025), particularly for fine-grained and clay-rich sandstones (SP3). Due to the availability and control on pre- and post-deformation CT images, we have used Porosity* for relative comparison of deformation-induced changes within the same sample, rather than for absolute or cross-sample quantitative porosity comparison.

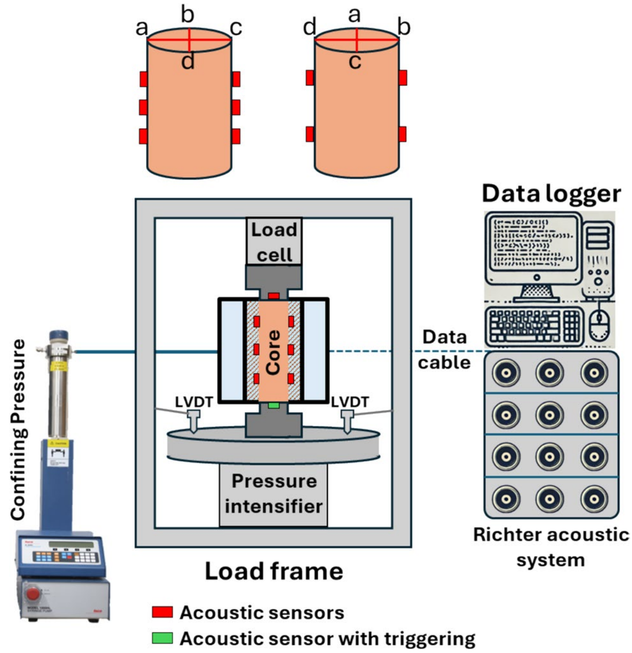

Fig. 1 Schematic of the core plug showing arrangement of acoustic sensors (top). Experimental setup used for this study containing the loading, active and passive sonic measurement system (bottom). The Richter multichannel acoustic system can act in both triggering and 'listening' mode

2.2 Experimental Protocol

An instrumented Hoek cell attached to a servo-controlled 500 kN uniaxial loading setup was used for the experiments in this study (Naderloo et al. 2023; Chandra and Barnhoorn 2025; Chandra et al. 2025). Confining stress was applied using a high-pressure ISCO-100DX syringe pump which can be programmed to maintain a constant flow or pressure gradient. The lower piston of the 500 kN load frame applied axial stress on the sample and was programmed to move vertically upward at a slow rate of 0.2 μm/s (4 μS/s). Vertical displacement of the piston was measured using two high-precision linear variable differential transformer (LVDT) sensors placed on either end of the Hoek cell (Fig. 1).

Resonant-type piezo sensors with a resonant frequency of 1 MHz, a diameter of 5 mm, and a thickness of 2 mm were embedded within the sleeve of the Hoek cell such that the core plug remains in contact with the sensors throughout testing (Fig. 1). A 12-sensor array was used for these experiments where ten sensors were placed radially, and two sensors were housed within the top and bottom pistons (oriented in the axial direction). A multichannel Richter acoustic system with a 16-bit analog to digital converter was used to detect AE during the experiments. Synchronous sampling from all input channels was performed using the ExStream software which also allows the sensors to alternate between 'listening' and triggering mode. In 'listening' mode, all sensors detect AE events from the specimen due to microcrack formation, whereas in 'triggering' mode, selected sensors transmit sonic pulses at a defined frequency, which travel through the sample and are recorded by the receiving sensors. For our experiments, we programmed one sensor (within the bottom piston) to trigger in 1-min intervals, with the remaining sensors acting as receivers

Table 1 Samples used for this study along with their origin and lithology

Seal peel	Formation	Plugs	Depth (m)	Porosity*	Porosity#	Lithological description
SP2	Cook	2	2680.25	13%	23%	Cross-bedded sandstones, medium grained Possibility of bioclasts or mud lining along lamina
SP3	Johansen	1	2726.87	7.2%	24%	Bioturbated sandstones, very fine grained. High resistivity indicative of bioclasts or mud-lined trace fossils
SP4	Johansen	2	2762.90	11.5%	32%	Massive sandstones, medium grained. No apparent structures or bioclasts

Porosity* values calculated from CT images (details in Sect. 3.3). Porosity# values are sourced from Griffiths et al. (2025)

throughout the experiment. The pulse frequency was set at 1 MHz, and the continuous waveforms were recorded with a 2 MHz sampling frequency throughout the experiment. A 5 V peak amplitude and 50 ohm (Ω), input impedance was set for recording the waveforms. We ensured that the peak amplitude did not exceed a 5 V threshold by performing a pencil lead break (PLB) test on each sensor (De Almeida et al. 2015). The InSite software suite (from ASC) was used to separate the waveforms from the active acoustic surveys from the passive monitoring data used to identify AE events.

Prior to axial loading, background noise levels were quantified during a static listening period, showing peak voltages typically below ~ 0.3–0.4 V. Based on this assessment, a conservative trigger threshold of 0.7 V was selected to ensure that only signals clearly exceeding the ambient electronic and mechanical noise were recorded. In addition, requiring a minimum of six sensors to exceed this threshold within a 480 µs time window effectively suppresses spurious triggers caused by electrical noise, single-sensor ringing, or local coupling effects. This multi-sensor coincidence criterion ensures that recorded events represent genuine, sample-generated acoustic emissions rather than system or environmental noise. A separate processing workflow was adopted for the active acoustic waveforms. Ultrasonic active acoustic waveforms were recorded in all 11 sensors, where 1 sensor acts as source; however, as our interest lies in the elastic properties along the axial direction, we analyzed only waveforms recorded in the sensor at the top piston for further processing. The ultrasonic waves were measured across the length of the sample, where the source, receiver, and their distance at each moment are known. The waveforms were exported to RadexPro for determining Vp, Vs, as well as picking *P* wave peak amplitude (Pamp) and *S* wave peak amplitudes (Samp). To calculate Pamp and Samp, we selected a 10 µs symmetric window around *P* and *S* wave arrival picks, respectively, and the absolute maximum amplitude was determined for each trace.

Prior to the tests, CT scans of the samples were performed (details in Sect. 2.3). The samples were saturated as received with reservoir brine and wrapped in cling film to retain moisture. After removing the film, the samples were vacuum saturated for 12 h with a brine solution (80 g/l NaCl solution) analogous to the in situ reservoir brine and then loaded into the Hoek cell. The tests were performed at a fixed confining stress; therefore, the samples were slowly brought to an equivalent isotropic stress manually before starting programmed axial loading and sonic recording. The in situ reservoir stresses at the EOS well and Aurora site (Thompson et al. 2022), and stress changes due to injection considering both pressure change and cooling provide the basis for the selected stress levels 1 and 3 MPa effective confining stresses for the test program. Effective horizontal stress is around 11 MPa for Cook and Johansen Formations. It should be noted that downhole injection pressure estimates from Aurora are not available to calculate the more exact stress changes from pore pressure; however, a maximum of 10 MPa can be the operational limit not to exceed the capacity of the caprock. This value is just for demonstration and is not necessarily used by operators at the Aurora site. The temperature changes of 80 °C and elastic properties of rock are used with the thermo-elastic equation (Fjær et al. 2008) to calculate the expected changes in stress induced from temperature (documented in Grande et al. 2024). The 1 and 3 MPa effective stresses were selected to bridge the gap in failure criteria between zero and the lowest effective confining stress of 5 MPa from previous tests (5, 10, and 15 MPa were used in previous tests). Sonic and mechanical data recording is terminated once core plugs fail axially, indicated by sudden drop in axial stress. A drainage line was connected to the perforated pistons to allow pore fluid drainage during compression.

2.3 Imaging and Image Processing

The samples were scanned with a Tescan CoreTom laboratory CT scanner before and after testing to assess the microstructural changes due to deformation. To scan the entire sample at the highest possible resolution, a voxel size of 15 µm was selected and the imaging was performed at 140 kV and 15 W with an exposure time of 3 s. Each constitutive image of the 3D volume was created by averaging three images to minimize instrumental artifacts. Post-reconstruction, the images were further processed in the ORS Dragonfly software to calculate porosity and visualize grain scale deformation. The raw images were first trimmed with a cylindrical mask to remove the contribution of the air and sample holder from the image volumes. Pores and cracks appear darker under X-ray illumination due to their low phase density. Utilizing an adaptive thresholding method based on greyscale values, the porosity (volumetric and per-slice) of each of the samples before and after the deformation experiments was calculated.

3 Results

3.1 Ultrasonic Velocity and Deformation

The objective of the tests was to assess the deformation behavior of highly porous reservoir core plugs at low confining pressure and simultaneously use active ultrasonic and AE measurements to monitor the physics of deformation. The experiments were named according to their seal peel, followed by the confining stress in each case (e.g., SP2-1 represents SP2 tested at 1 MPa confinement). Figure 2 shows the axial stress, axial Vp and Vs, plotted against axial strain.

The stress–strain profile of the sandstones up to the point of failure indicates that higher confining stress leads to a higher peak load (Fig. 2) and also a slightly higher Young's modulus (*E*). For SP4-3, between yield point and failure, there is a period where axial stress remains unchanged, which might result from local stress relaxation prior to macroscopic failure in the specimen.

The axial Vp and Vs show constant increase until the elastic–plastic transition zone, where microcracks start to form, leading to increased wave attenuation and a steep decrease in the velocities. At failure, the drop in Vs is more rapid compared to Vp, especially at higher confining stresses, where Vs reaches values close to the isotropic stress condition (Table 2). The more rapid decrease in Vs compared to Vp reflects the higher sensitivity of shear waves to reductions in shear stiffness. Vs is directly controlled by the shear modulus, which is preferentially degraded by shear microcracking, specifically caused by cracks appearing parallel to the loading direction, frictional sliding, and loss of intergranular contact during inelastic deformation. In contrast, Vp depends on both bulk and shear moduli, and is therefore less sensitive to early damage. As a result, deformation mechanisms dominated by shear and grain-boundary processes lead to an earlier and steeper decline in Vs.

A similar trend is observed for Pamp and Samp, both increasing until the axial stress surpasses the elastic deformation limit (Fig. 3). From this point onward, both Pamp and Samp continue to decrease. For tests performed at low confinement, the drop in Samp is a bit delayed compared to Pamp. Since *S* wave transducers were used as source and receiver, the magnitudes of Samp are higher than those of Pamp. When samples from the same seal peel are tested under different confining stresses (SP2-1, SP2-3 and SP4-1,

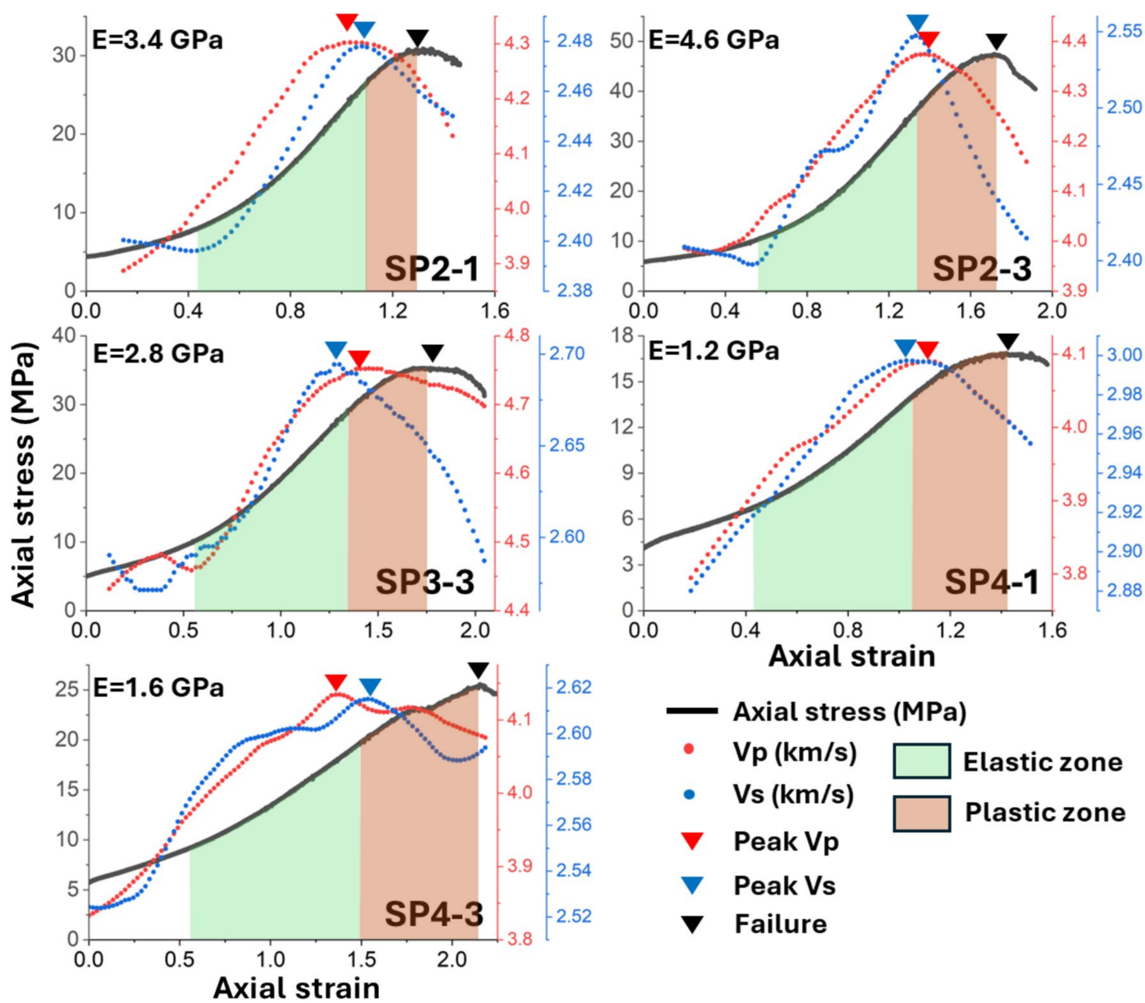

Fig. 2 Change in Vp and Vs as a function of stress change till the point of failure during the triaxial tests. Peak Vp and Vs are marked with triangles for each experiment. Numbers after the dash (–) of each test indicate corresponding confining stresses. Young's modulus (*E*), as well as elastic and plastic deformation zones for each experiment, is also indicated. The microcrack closure zone precedes elastic deformation

Table 2 Vp and Vs prior to axial loading (isotropic stress), at the peak stress (yield point,) and after failure for each experiment (all values in km/s)

Sample ID	At start	Peak	After failure
SP2-1	Vp: 3.88	Vp: 4.31	Vp: 4.13
	Vs: 2.4	Vs: 2.47	Vs: 2.45
SP2-3	Vp: 4.0	Vp: 4.37	Vp: 4.16
	Vs: 2.41	Vs: 2.54	Vs: 2.41
SP3-3	Vp: 4.43	Vp: 4.75	Vp: 4.69
	Vs: 2.59	Vs: 2.7	Vs: 2.58
SP4-1	Vp: 3.79	Vp: 4.09	Vp: 3.98
	Vs: 2.88	Vs: 2.99	Vs: 2.95
SP4-3	Vp: 3.83	Vp: 4.13	Vp: 4.07
	Vs:2.52	Vs: 2.61	Vs: 2.59

SP4-3), lower confinement results in lower velocities and amplitudes.

3.2 Acoustic Emissions and Deformation

As described in Sect. 2, continuous monitoring of AE was performed using an array of 12 sensors during the failure experiments. During each experiment, a greater number of microseismic events were recorded with increasing differential stress [axial stress (σ_1)-confining stress (σ_3)] (Fig. 4). Across experiments, a significantly higher number of cumulative events are observed at higher confinement.

The rate of events and their magnitudes increase exponentially after the yield point, which correlates with the decreasing trend in shear wave velocity. For the SP3-3 sample, the number of events is significantly lower compared to the other tests, even at higher confinement. During the experiments performed, we observe close correlation between ultrasonic shear wave velocity, event counts, as well as energy of the events. Here, the acoustic energy of each event is calculated from their amplitude (Khazaei et al. 2015; Grosse et al. 2022; Naderloo et al. 2023) (Eq. 1).

$$E_i = \frac{1}{R}\int_{t_0}^{t_1} V_i(t)^2 \mathrm{d}t, \tag{1}$$

Where V_i is the voltage of each trace point that exceeds the threshold amplitude; t_0 and t_1 are the starting and ending times of the transient voltage record; and R is equal to 50 Ω representing the input impedance of the AE system. In most cases, the peak in Vs appears earlier than the events of higher energy (also change in the AE rates), signifying that the mechanism during initial plastic deformation is primarily aseismic (silent in terms of large energy events), which leads to more high-energy (large magnitude) events as deformation progresses (Fig. 5). At higher confinement (for SP2 and SP4), the maximum energy released per event is lower, whereas the events are more distributed temporally. The reduction in peak AE energy with increasing confinement can also be interpreted within the framework of the well-established inverse relationship between *b*-value and deviatoric stress (Scholz 1968; Amitrano 2003; Goebel, et al. 2013). As rocks approach failure under low confinement, the deviatoric stress increases more rapidly, which is typically associated with a decrease in *b*-value and a relative enrichment of larger-magnitude events. Laboratory acoustic emission studies have demonstrated that *b*-value systematically decreases as differential stress approaches failure, reflecting an increasing contribution from larger source dimensions and higher stress drops (Scholz 1968; Goebel et al. 2013). Mechanistically, low-confinement conditions favor localized brittle processes such as rapid grain-boundary slip and enhanced tensile microcrack propagation (Wong et al. 1997; Baud et al. 2000). These processes promote crack coalescence into discrete failure planes, generating fewer but higher-energy AE events and consequently lower *b*-values. In contrast, higher confinement suppresses tensile opening and promotes distributed cataclastic deformation and pore collapse (Wong et al. 1997; Baud et al. 2000; Amitrano 2003; Huang et al. 2021). Under such conditions, strain is partitioned into numerous small-scale failure episodes characterized by reduced stress drops and limited source dimensions. Experimental studies on sandstones have shown that increasing confining pressure results in higher *b*-values and suppression of large-magnitude AE events, consistent with a transition toward more distributed damage (Huang et al. 2021; Yang et al. 2018). Consequently, stored elastic energy is released more incrementally through many smaller events and frictional dissipation rather than a few large intergranular fracture or slip events, leading to lower maximum energy per event despite higher cumulative event counts. It can also be observed that the acoustic emission events do not occur immediately after the onset of axial loading, which is expected, since the events in acoustic emission originates from mostly irreversible damage (grain crushing or crack formation).

Figure 5 also indicates that the increase in ultrasonic Vs starts earlier than the AE events. Comparing energy released during each AE event against the change in Vs over time shows that the drop in Vs precedes the higher-energy events. Only in case of SP2-3, trend reversal in Vs and the highest-energy event occurred concurrently. Since energy emitted during deformation is directly proportional to the magnitude of a seismic event, the onset of plastic deformation does not directly translate to high seismicity. Interestingly, the maximum energy of each event generally decreases with an increase in confinement. It is also observed from the slope

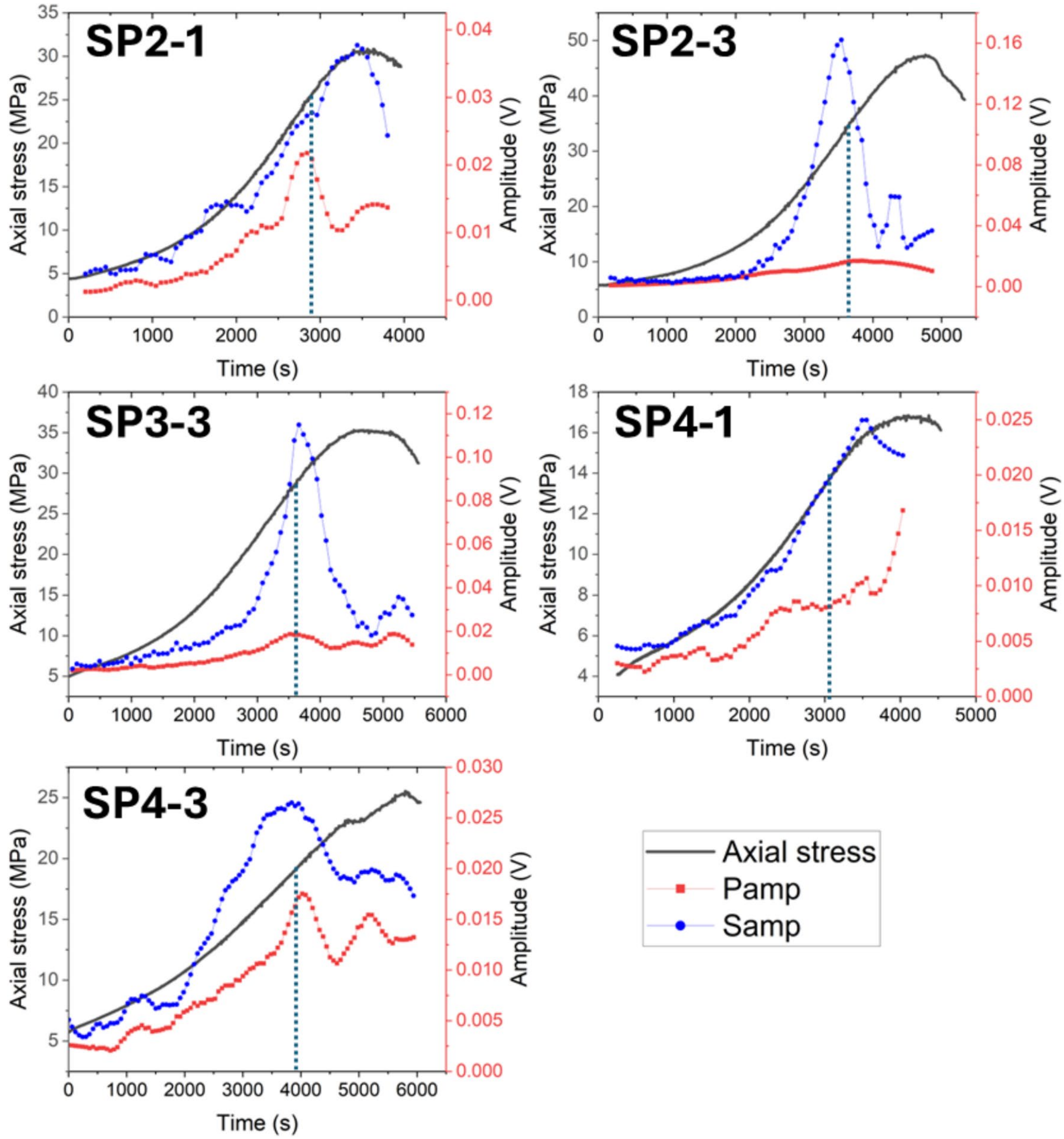

Fig. 3 Change in Pamp and Samp as a function of stress change till the point of failure during the triaxial tests. Pamp in *V* (blue) and Samp in *V* (red) are plotted to the same scale. The vertical blue dotted lines represent the yield point for each test (Color figure online)

of the cumulative event (Fig. 5) that since the onset of the highest-energy event, the event rate increases drastically.

3.3 3D X-ray Imaging Pre- and Post-deformation

Images of the samples before and after deformation helped us get an idea of the microstructures including heterogeneity, grain size distribution, grain angularity, and porosity. One objective of this exercise was to compare the change in porosity after deformation. In CT image processing, it is difficult to decouple the effect of porosity and cracks, since they both exhibit similar grayscale values. In context of fluid flow, these smaller and larger cracks also contribute as connected pores. Along the primary fault plane, there is an obvious increase in porosity due to the generation of larger cracks and distributed microcracks (Fig. 6). Any change in porosity in the bulk volume is contributed by grain crushing, grain reorientation, smaller cracks, and pore collapse. Determining grain rotation is difficult due to challenges in image registration pre- and post-deformation. However, a significant increase in porosity of the bulk rock mass was observed post-failure with increasing confinement (Table 3). Note that the scan resolution (15 µm) is a limiting factor for porosity estimation, and any pores smaller than 30 µm will not be

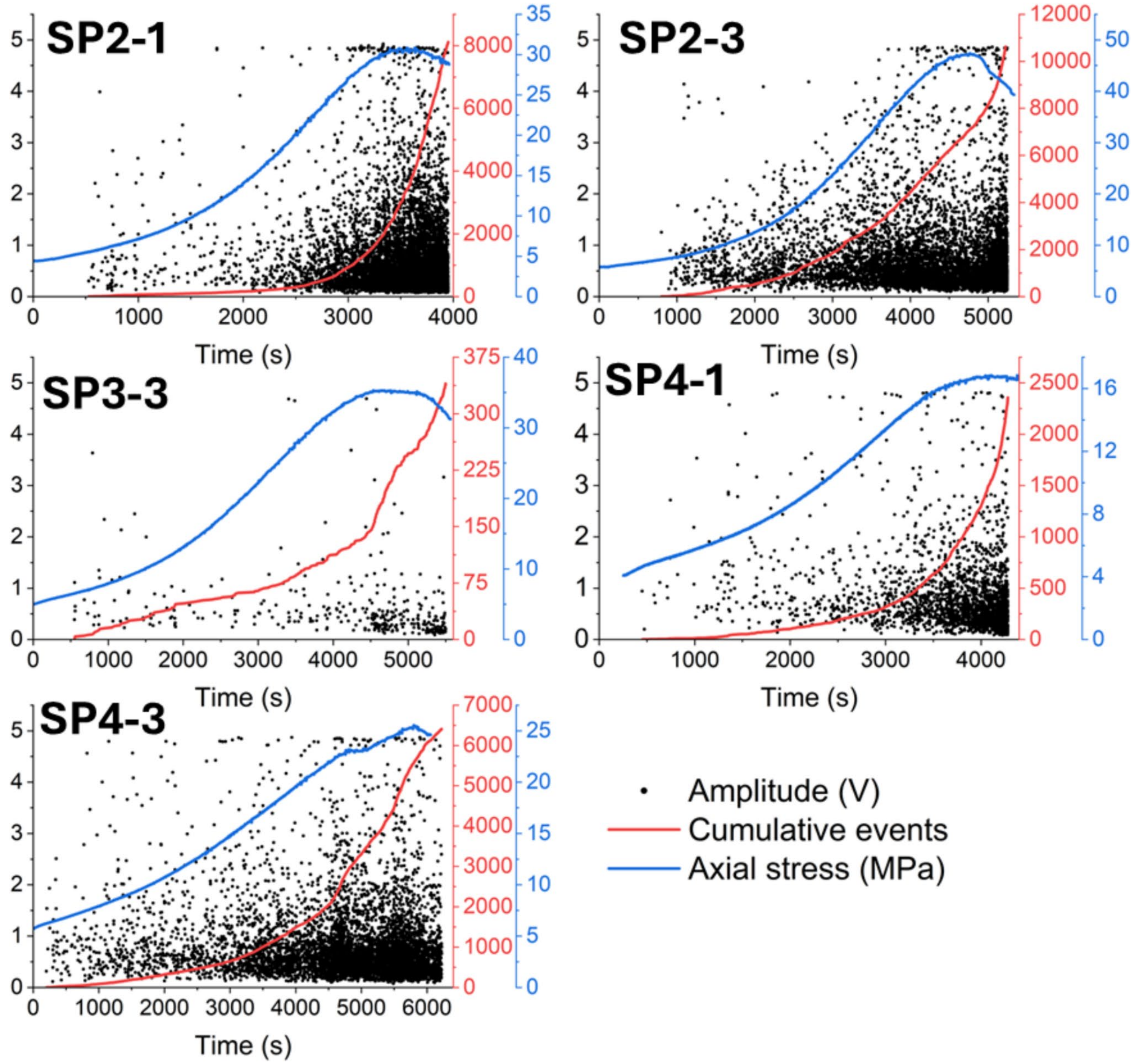

Fig. 4 Amplitude of each acoustic emission events recorded during the failure experiments and evolution of cumulative events over time

reflected in the porosity calculation, which causes a significant underestimation compared to the porosity reported in Griffiths et al. (2025) (Table 1). As noted in Sect. 2.1, the limit in scan resolution leads to systematic underestimation of bulk porosity. Nevertheless, the CT data reliably capture relative porosity changes and spatial damage patterns, which are the focus of the post-deformation imaging analysis. It is evident from Fig. 6 that failure at higher confinement contributes to diffused crack and more grain crushing, whereas at lower confinement, the crack influence zone is smaller, and cracks mostly follow grain boundaries.

Post-failure samples were unloaded by slowly releasing stresses and carefully dismounting samples from the Hoek cell to minimize alteration of porosity by improper handling. The samples were intact after unloading and immediately imaged with the CT scanner (Supplementary Fig. A1). However, as the stresses on the core plug are removed, the matrix 'relaxes', causing the smaller cracks and failure surfaces to open up which results in a higher porosity estimation. It is also evident that SP3 has significantly smaller grain and pore sizes compared to SP2 and SP4. SP3 has clasts of bigger grains embedded within the matrix, which influences the deformation behavior (lack of porosity increase between slice 350–400).

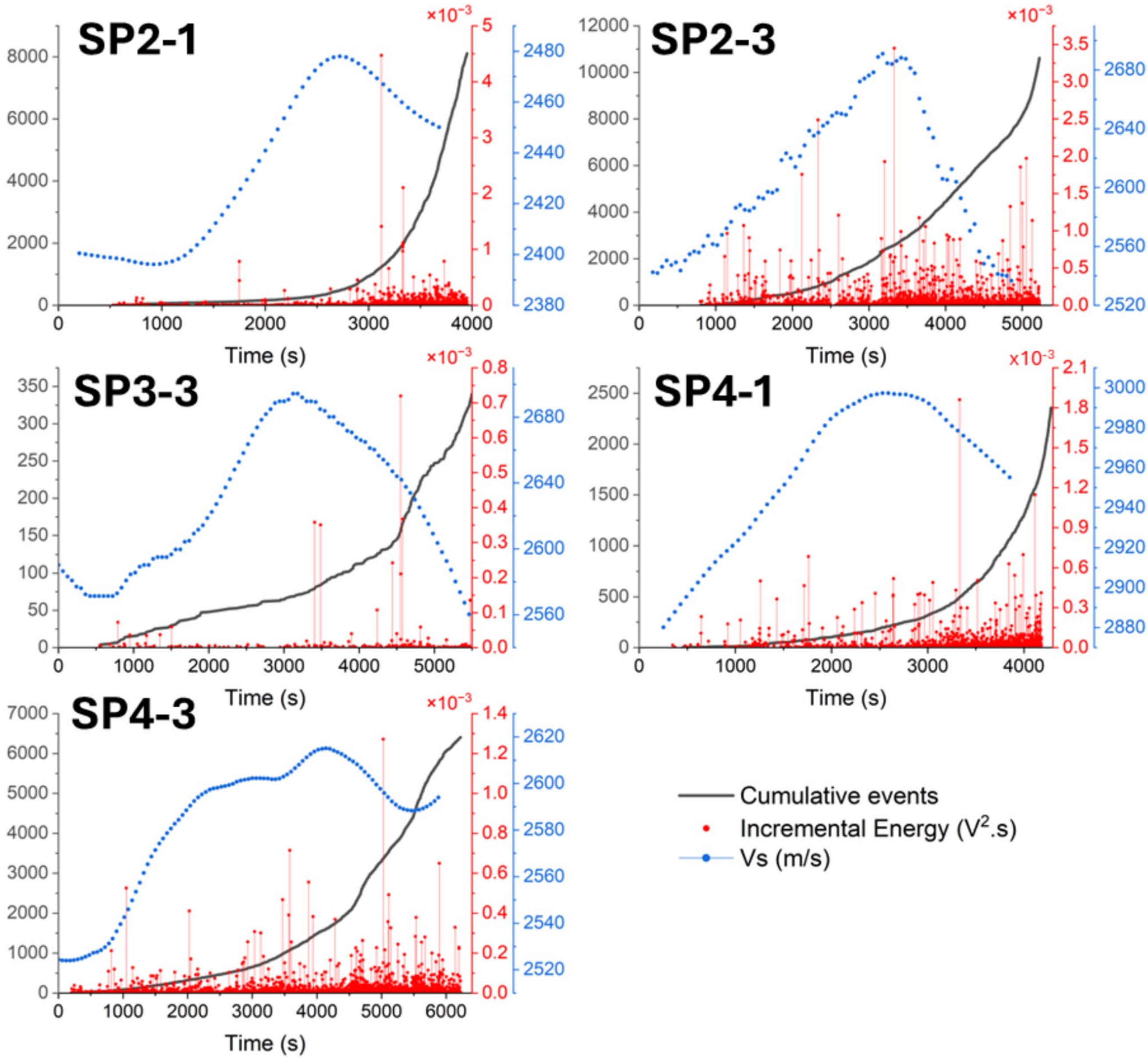

Fig. 5 Change in Vs with increase in cumulative events during the deformation, also highlighting energy released by each event before and after velocity reversal

SP4 has coarser and more angular grains than SP2, however, both are mostly homogeneous, unlike SP3.

4 Discussion

4.1 Failure Behavior as a Function of Confinement

Grande et al. (2024) performed triaxial failure experiments on the same set of samples at higher confinements (5, 10, and 15 MPa) and found a linear correlation between confining stress and shear stress at failure. However, combining the low-confinement experimental data (from this study) with their dataset, we can see a non-linear behavior between confining and shear stress at failure, which is also highlighted in other studies for different rock types (Wong et al. 1997; Baud et al. 2000). In classical Mohr–Coulomb assumption, the failure envelope is often assumed to be linear, which does not hold true for porous reservoir rocks. Sandstones and limestones with higher porosity (11–35%) require much lower mean stress to undergo pore collapse than low-porosity rocks (Baud et al. 2000), and once pore collapse initiates, the material behavior changes from dilatant to compactive, causing shear-enhanced compaction. The traditional linear

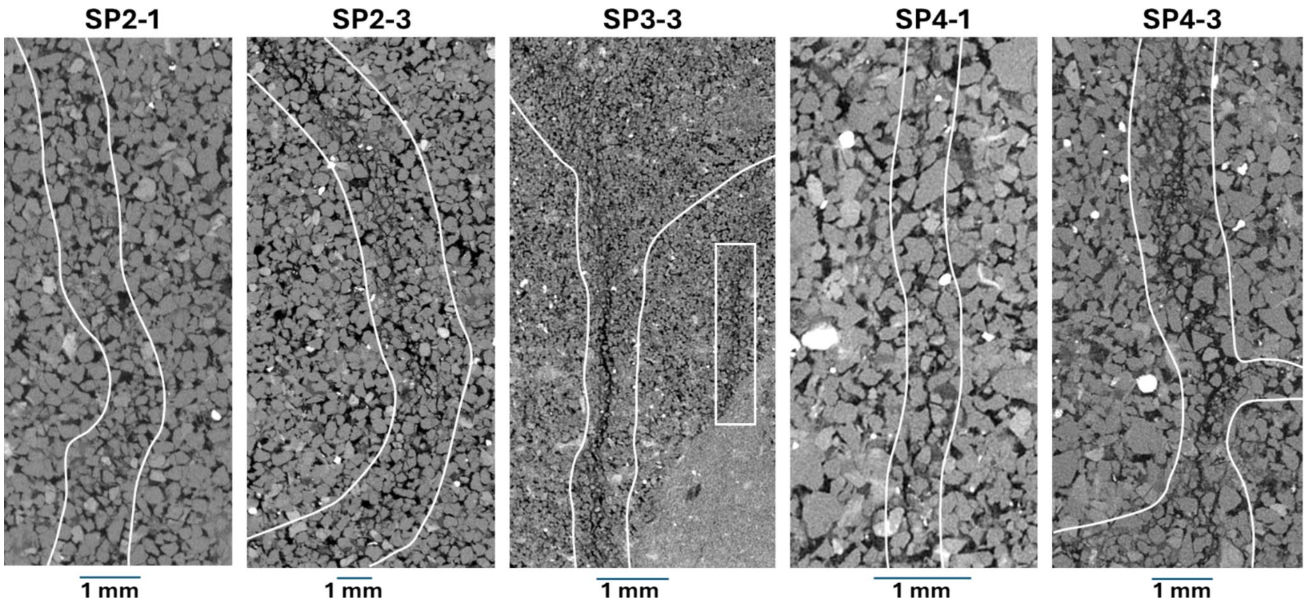

Fig. 6 Snapshot of X-ray CT images for all samples post-failure highlighting a small section of primary crack zones (bounded by white lines)

failure criterion (Mohr–Coulomb) holds true when the deformation mechanism is primarily controlled by shear deformation and frictional sliding, whereas for highly porous rocks, at low confinement, pore collapse plays a dominant role, which causes failure at lower shear stresses than expected, causing deviation from linearity. Therefore, deformation in the low-confinement regime can be more appropriately modeled using the Hoek–Brown criterion, where parameters such as intact rock constant, geological strength index (GSI), and disturbance factor represent rock type and porosity more accurately (Hoek et al. 2002) (Fig. 7). Without considering the low-confinement data points, the studied samples show a linear failure envelope as reported in Grande et al. (2024). Similarly, other porous sandstones (Wong et al. 1997), where low-confinement (< 5 MPa) tests were not performed, show a linear failure envelope (Fig. 7).

This deviation from linearity in Fig. 7 at low confinement underlines the requirement of comprehensive experimental study to understand the complex deformation behavior of reservoirs while modeling the long-term viability of safe storage. Injection of CO_2 in the reservoir reduces effective stresses, which causes deviation of the failure criterion from linearity (Fig. 7). Importantly, pore pressure increase during injection shifts the reservoir stress state into a low effective stress regime where failure behavior becomes strongly non-linear. Our results show that this transition is accompanied by early irreversible deformation and pronounced changes in elastic properties, well before macroscopic failure (also observed by McBeck et al. 2026), underscoring the need to account for non-linear stress–strain behavior when defining safe injection pressures.

4.2 Combining Ultrasonic Velocity and Microseismicity: Improved Monitoring

Laboratory experiments have shown that crack formation in porous sandstones is usually seismic, since it is governed by local stress concentrations and is abrupt in nature (Zhao et al. 2021). Depending on the stress configuration, mineralogy, and pore fluid saturation, cracks once formed seismically can grow aseismically below critical stress intensity and at much slower velocities than dynamic rupture velocity (Smeraglia et al. 2017), as seen in post-yield deformation behavior in our experiments (Fig. 8).

Laboratory studies coupled with time lapse CT imaging indicates that around 1/3rd of the bulk shear fracture energy is contributed by aseismic deformation including crack and grain rotation (Cartwright-Taylor et al. 2022). Their experiments prove that seismic events with higher energy come from small local strains and vice versa. In our experiments (Fig. 5), after the onset of plastic deformation, although there is a considerable increase in the number of events, the energy of individual events does not increase drastically compared to the ones observed in an elastic deformation zone. There are few events after the onset of plasticity which are of exceptionally higher energy, but these events precede the point of failure, which indicates the possibility of them originating from small local strains. At higher confinement, the number of high-energy events increases as failure is accommodated by a more spatially distributed system of small cracks, which form under lower local strain but accumulate collectively to release larger seismic energy (Fig. 6). Post-failure events recorded at the end of each experiment

Table 3 Change in bulk porosity and porosity across the length of the studied core plugs before and after failure experiments

Sample ID	Porosity (pre-deformation)	Porosity (post-deformation)	Porosity profile
SP2	13%	SP2-1: 24.2% SP2-3: 25.3%	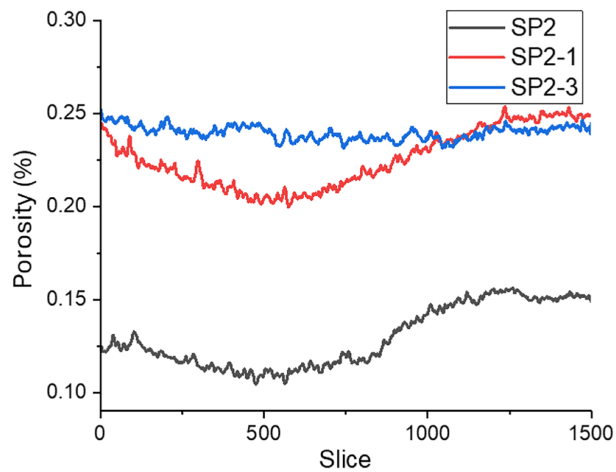
SP3	7.2%	SP3-3: 11.32%	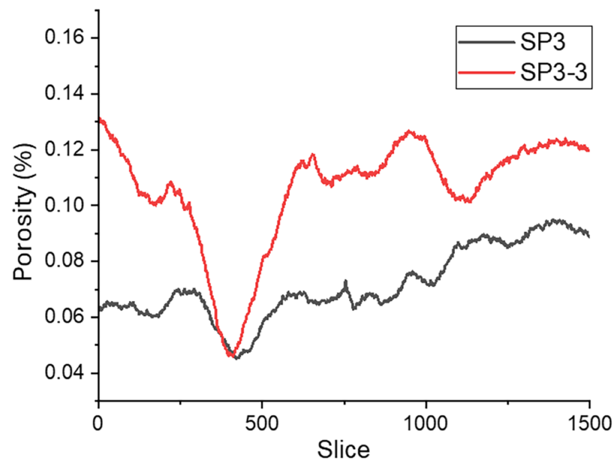
SP4	11.5%	SP4-1: 24.4% SP4-3: 25.6%	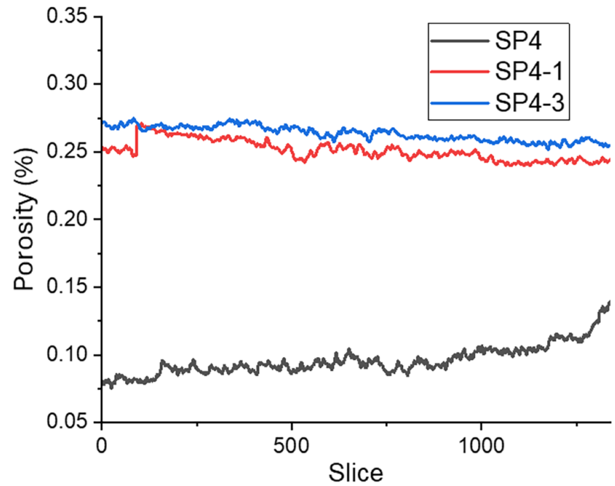

The black, red, and blue lines indicate vertical porosity profile (slices perpendicular to the axial loading)

are, however, of higher energy, since they are not produced by new crack generation, but rather contributed by friction along a pre-existing plane of rupture.

A combined overview of rate of ultrasonic velocity change and acoustic event rate indicates that dV (rate of velocity) drops sharply as the sample approaches the linear deformation limit, whereas the rate of microseismicity starts increasing after d*V* approaches zero (Fig. 8). For tests conducted at higher confinement, d*V* is smaller than that at lower confinement, whereas Vp and Vs are higher throughout elastic loading (Fig. 2). At higher confinement, the pore space in the plugs is already more compressed hydrostatically, which results in a higher net velocity throughout the experiment, but a smaller change in d*V* during elastic deformation (Chandra et al. 2025). Based on the drop in d*V*, the event rate, and energy of each event, we defined three distinct zones of deformation relevant for subsurface operations (Fig. 8). In the green zone, we have a low and constant event rate, which is primarily due to grain rotation and closure of pre-existing cracks. At higher confinement, the event rate is also higher; however, energy released during each event is lower. Following the initial crack-closure (seating) stage, Vp and Vs increase approximately linearly with strain; accordingly, d*V* is positive but typically decreases toward a near-constant value as the rock frame stiffens. As damage initiates near the elastic limit, d*V* approaches zero and then becomes negative at velocity reversal, coincident with a marked increase in AE rate (Fig A2). For the sake of easier representation (Fig. 8), we have only used the magnitude of dV; therefore, increasing values of d*V* below 0 is also represented as positive. This drop in d*V* (both dVp and dVs used as indicators) signifies the limit of linear deformation and thus colored in yellow (early-warning zone). Beyond the yield stress, the growth of stable microcracks triggers higher event rates and higher-energy events, finally leading to failure. Therefore, this zone is marked in red (critical zone). This traffic light scheme complements the one proposed by Chandra et al. (2025), where only active acoustic indicators were used. Event rate as an exclusive indicator would only detect irreversible deformation after its onset. Using microseismic energy as an indicator would be ineffective, since most high-energy events occur much later after the onset of irreversible deformation.

In all tests, the reversal/decline in Vs occurs prior to the appearance of the highest-energy AE events (Fig. 5), indicating that the earliest inelastic deformation is partly aseismic with limited radiated energy. We interpret this phase as dominated by progressive loss of shear stiffness through stable microcrack growth and intergranular processes including grain-boundary sliding, frictional microslip, and contact debonding which can result in Vs attenuation while producing only low-energy or spatially distributed AE. Under higher confinement, the CT observations show a wider, more distributed damage zone with pervasive grain fragmentation and microcracking (Fig. 6), consistent with cataclastic deformation and pore collapse-assisted compaction. Such distributed damage is expected to evolve through many small-scale contact failures and crushing episodes, delaying the emergence of distinct, high-energy events associated with rapid crack coalescence or localized slip. In contrast, at low confinement, damage localizes earlier into a narrower fracture process zone (Fig. 6), promoting fewer but more energetic events once a dominant rupture surface develops. The confinement cases characterized by a wider damage zone in CT (Fig. 6) also exhibit a longer interval between Vs reversal and the onset of the highest-energy AE events (Fig. 5), consistent with distributed cataclastic damage accumulating aseismically before macroscopic localization.

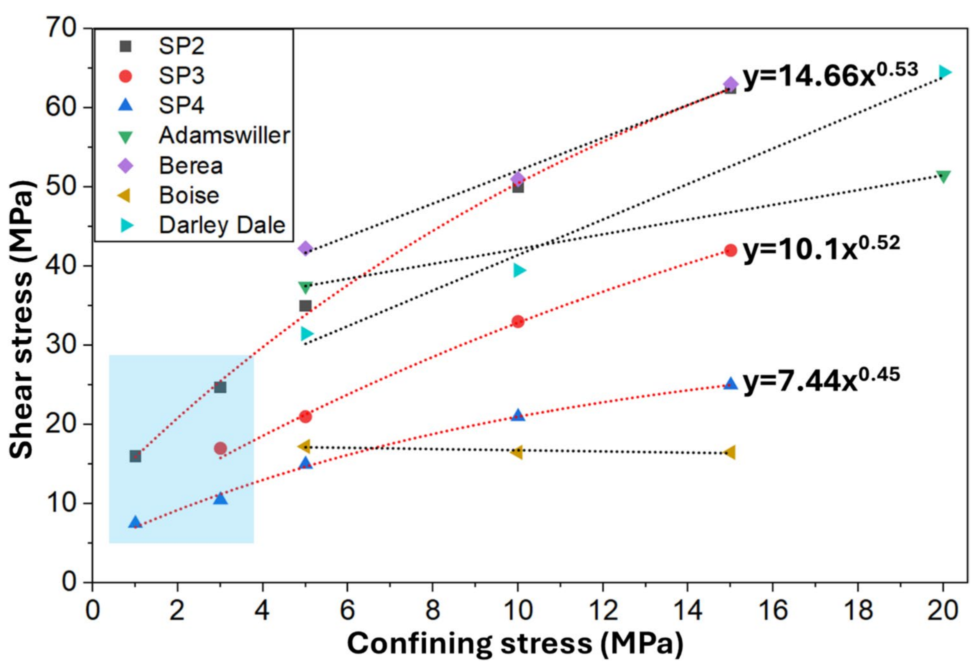

Fig. 7 Criterion for shear failure for porous sandstones at different confinements. The data points within the blue box are from this study, whereas the high-confinement tests for the same samples (SP2, SP3, SP4) were performed by Grande et al. (2024). Rest of the data points are collected from Wong et al. (1997). The red dotted lines represent exponential fits for SP2, SP3, SP4, while the black dotted lines represent linear fits of corresponding samples tested at different confinements (Color figure online)

4.3 Correlating Active and Passive Acoustic Observations as a Function of Stress

We attempted to analyze if there is any relationship between the increase in cumulative events (CE) with Vp and Vs. Ideally, CE is positively related to crack formation and spreading, whereas crack formation attenuates wave propagation, causing a drop in velocities. To determine the relationships between CE increase and velocity decay due to plastic deformation before failure, we chose the interval between yield point and peak stress (Fig. 9).

Vp and Vs peaks around the same time, which is a bit earlier than the time when CE increases rapidly. From the linear fits, we derived correlations that govern Vp and Vs decrease as a function of time. In brittle regimes approaching instability, crack interaction leads to stress amplification at crack tips, producing positive feedback in damage evolution. Continuum damage mechanics and fracture models predict accelerating crack growth, commonly expressed as exponential or time-to-failure power-law acceleration of acoustic emission rate (Lockner et al. 1991; Fortin et al. 2009). In contrast, ultrasonic velocity decreases approximately linearly with accumulated crack density, as predicted by effective medium theory (Walsh 1965; O'Connell and Budiansky 1974). Eliminating time between these relations yields a logarithmic dependence of velocity on cumulative event count. Therefore, an lnCE–V formulation is more consistent with fracture physics in accelerating damage regimes than CE–V assumption, which implicitly neglects crack interaction and critical acceleration effects. Similarly, an exponential fitting between the increase in CE and time were determined for each experiment. Since these experiments maintain a constant deformation rate over time, strain and time can be interchanged in the following formulations. Let us assume the exponential fit of CE versus time is represented as

$$\mathrm{CE} = Ae^{R_0 t} + c_1, \tag{2}$$

$$t = \frac{1}{R_0}\ln\left(\frac{\mathrm{CE} - c_1}{A}\right), \tag{3}$$

where A is the background cumulative event (above baseline) at the start of the fitting window, R_0 is the growth rate of events, t is the time (between yield point and peak axial stress), and c_1 is the extrapolated baseline cumulative event at t_0. Similarly, the linear best fit of time versus $V_{p,s}$ can be expressed as

$$V_{p,s} = -m_{p,s}t + c. \tag{4}$$

Replacing t from Eq. 3,

$$V_{p,s} = c - \frac{m_{p,s}}{R_0}\ln\left(\frac{\mathrm{CE} - c_1}{A}\right), \tag{5}$$

$$\begin{aligned} V_{p,s} &= c - \frac{m_{p,s}}{R_0}\left[\ln\left(\mathrm{CE} - c_1\right) - \ln(A)\right] \\ &= \left(c + \frac{m_{p,s}}{R_0}\ln A\right) - \frac{m_{p,s}}{R_0}\ln\left(\mathrm{CE} - c_1\right), \end{aligned} \tag{6}$$

where $m_{p,s}$ is the slope and $c_{p,s}$ is the intercept of the linear fit for velocity–time relationship. The resulting empirical relationships between CE and velocities for each experiment are displayed in Table 4. The relationship effectively reduces to a linear function where $\left(c + \frac{m_{p,s}}{R_0}\ln A\right)$ is the intercept and $\frac{m_{p,s}}{R_0}$ is the sensitivity factor. For tests done at low confinement, we observe a higher R_0 and $m_{p,s}$ and lower A. However, we find that R_0 is more sensitive to confinement compared to the slope of velocity change, resulting in a significantly higher value of sensitivity factor $\left(\frac{m_{p,s}}{R_0}\right)$ at higher confinement. We can ignore c_1, due to the assumption that background microseismicity is non-existent at t_0. In the intercept, $\left(\frac{m_{p,s}}{R_0}\ln A\right)$ plays the most influential role. Although c is higher at higher confinement, the difference in this case (comparing 1 and 3 MPa) is not as significant. Since these equations are derived from the plastic deformation zone, $CE, V \subseteq \mathbb{N}$.

The confinement dependence of the velocity–AE relationship reflects both (i) the kinetics of event accumulation and (ii) the sensitivity of elastic moduli to evolving microdamage. Because CE accelerates toward failure, we fit CE with an exponential law and express the velocity correlation in logarithmic form, $V_{p,s} = \alpha_{p,s}\ln(\mathrm{CE}) + \beta_{p,s}$. Here, $\alpha = \mathrm{d}V/d\ln CE$ measures the velocity drop associated with an exponential increase in event count and is controlled by the ratio between the linear velocity degradation rate and the AE acceleration rate. Higher confinement promotes cataclastic deformation and a wider damage zone, leading to progressive reduction in effective moduli sampled by the ultrasonic ray path; this is reflected in stronger sensitivity of V_s relative to V_p. In contrast, low-confinement deformation localizes into narrower fracture bands, and CE accelerates more strongly near peak stress, making linear V–lnCE slopes sensitive to the chosen window. The steeper slopes observed for SP3-3 are consistent with its lower porosity and fine-grained/heterogeneous fabric, which can enhance stiffness degradation once damage initiates, while threshold-limited AE detection may also steepen the apparent V–lnCE dependence. Accordingly, these coefficients should be treated as calibration parameters tied to stress path and microstructure rather than universal constants.

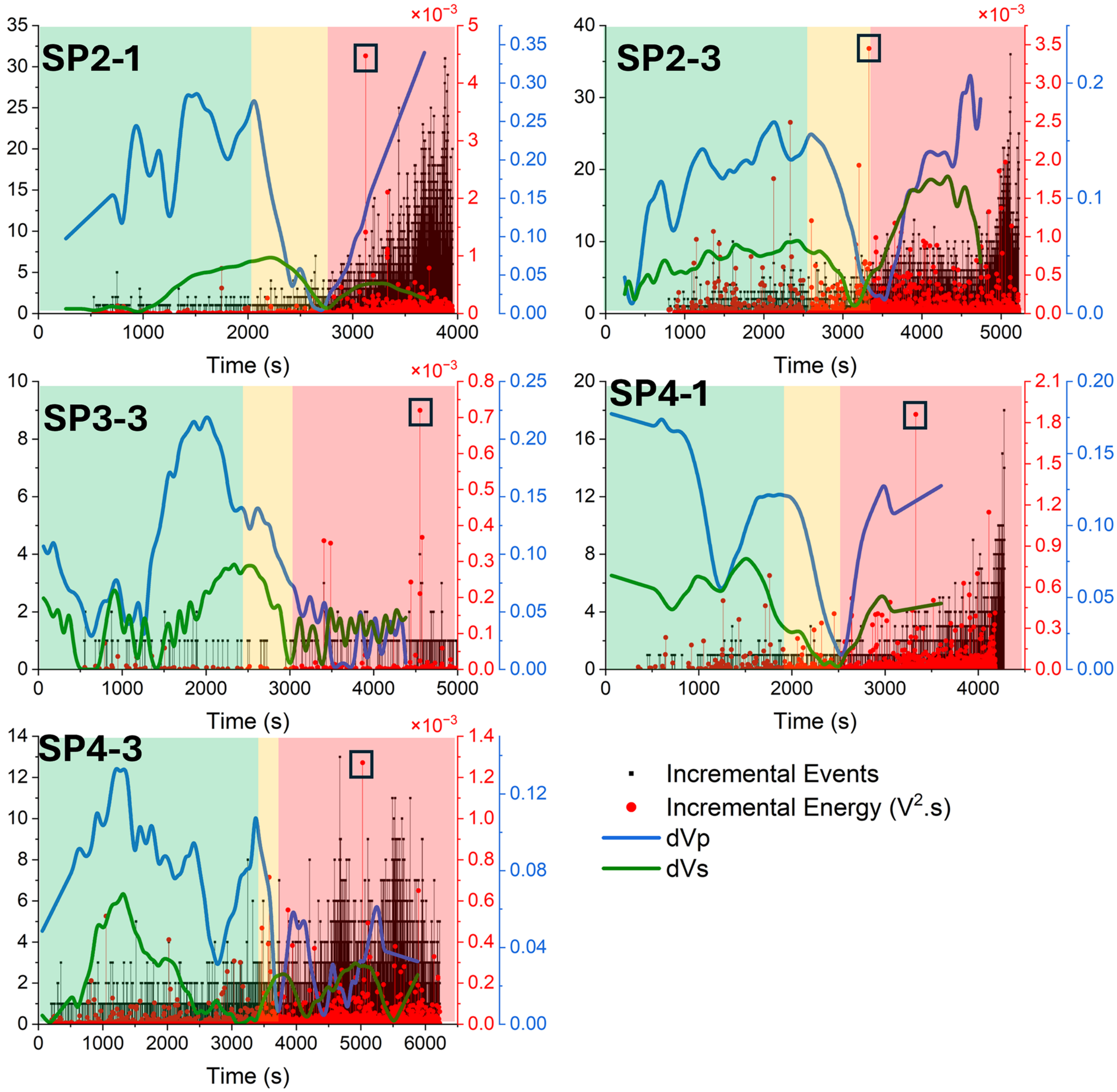

Fig. 8 Sensitive deformation zones marked based on rate of change of ultrasonic velocity (|d*V*|), acoustic event rate and energy emitted over time. Green, yellow, and red zones mark normal, early-warning, and critical zones, respectively. For the sake of easier representation, we have only used the magnitude of d*V*; therefore, increasing the values of d*V* below 0 is also represented as positive (Color figure online)

These relationships provide an indication that a physics-based correlation might exist between microseismic and velocity monitoring for subsurface CO_2 injection operations. However, such correlations should be determined using laboratory experiments on a case-by-case basis, as multiple factors including grain size, mineralogy, porosity, heterogeneity, fluid composition, etc., can cause deviation from the proposed relationships. Site-specific calibration can be obtained by combining (i) core-scale triaxial tests under representative effective stress paths, (ii) concurrent AE monitoring to build CE–strain (or CE–stress) relations, and (iii) active ultrasonic measurements to quantify the corresponding velocity/attenuation evolution. The resulting calibrated coefficients can then be mapped to field observables by matching the relevant stress-path regime and by using baseline sonic-log to constrain intercepts. Where field microseismicity is sparse, active time-lapse velocity changes can still be interpreted within the calibrated envelope. Conversely,

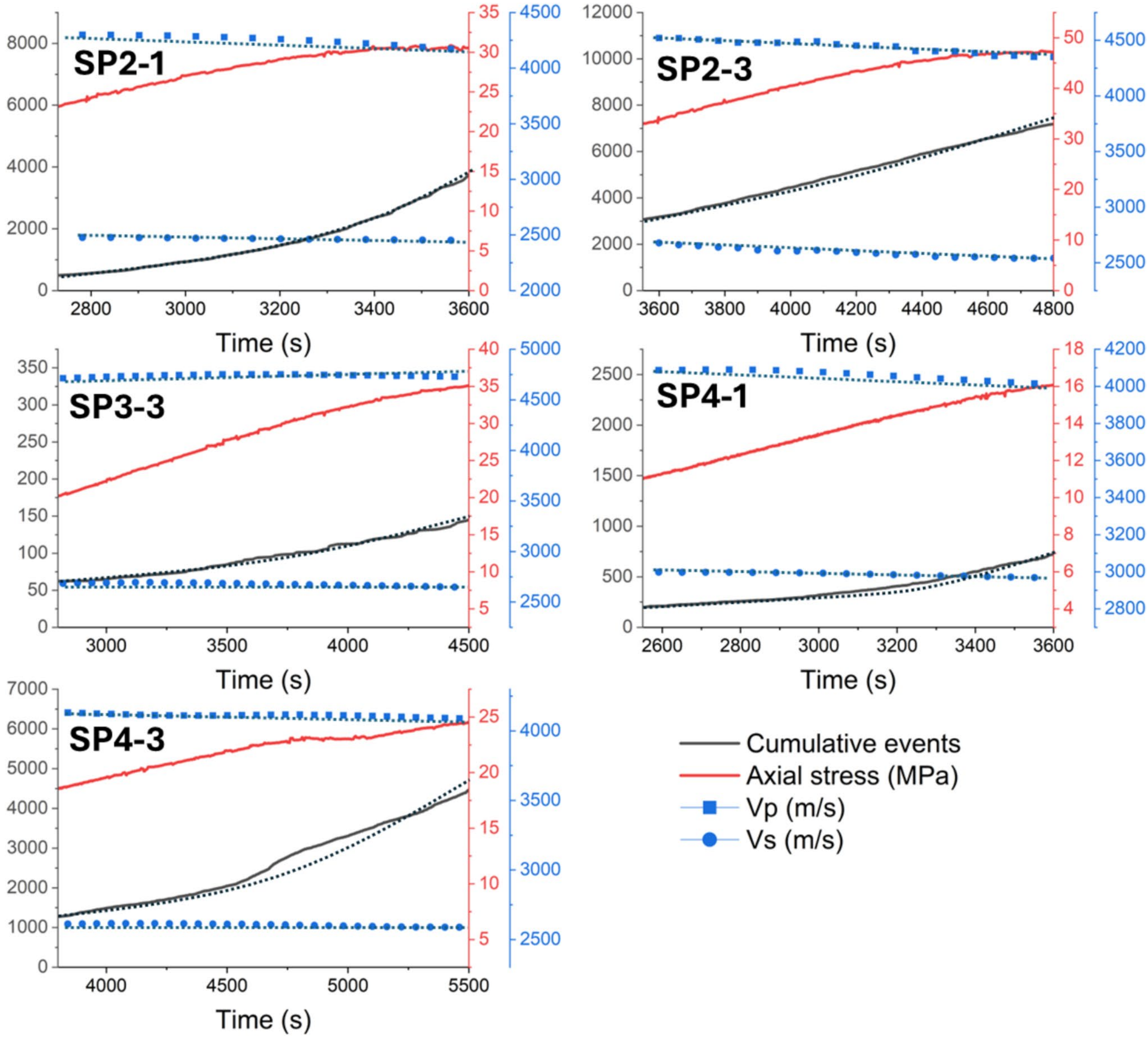

Fig. 9 Correlation between increase in microseismic events and velocity decay due to plastic deformation (interval between yield point and peak axial stress). The blue dotted lines represent the linear fit of the wave velocities, whereas the black dotted lines represent exponential fit of cumulative events with respect to time (Color figure online)

where active surveys are limited, microseismic event trends can be interpreted in terms of expected stiffness degradation within the same calibrated regime.

4.4 Frequency-Dependent Attenuation due to Fracture-Induced Scattering

There are multiple lines of evidence for understanding deformation of sandstones and other crystalline rocks during laboratory tests using ultrasonic waves. Application of ultrasonic and seismic waves to understand deformation behavior in sandstones and other rock material is extensively seen in laboratory experiments, where parameters like *P* and *S* wave velocity, their amplitudes, and coda are utilized to characterize deformation behavior (Lockner et al. 1991; Fortin et al. 2009; Barnhoorn et al. 2018; Sang et al. 2020; Janssen et al. 2023; Lozovyi et al. 2024; Chandra et al. 2025). Similar to wave velocity and amplitudes, the frequency response also changes as a function of deformation (Li et al. 2023). In our experiments, we observed that high-frequency components of the waveforms generally arrive earlier and are less affected by evolving deformation, whereas lower-frequency components exhibit greater sensitivity to damage. We use the term frequency-dependent attenuation (spectral reshaping) to

Table 4 Relationship between compressional and shear wave velocities and acoustic emission during triaxial deformation tests

Test ID	Empirical relationship
SP2-1	$V_p = -138\ln(\text{CE}) + 4342$
	$V_s = -146\ln(\text{CE}) + 2646$
SP2-3	$V_p = -746\ln(\text{CE}) + 5246$
	$V_s = -781\ln(\text{CE}) + 3531$
SP3-3	$V_p = -236\ln(\text{CE}) + 4986$
	$V_s = -251\ln(\text{CE}) + 2901$
SP4-1	$V_p = -54\ln(\text{CE}) + 4154$
	$V_s = -61\ln(\text{CE}) + 3111$
SP4-3	$V_p = -98\ln(\text{CE}) + 4248$
	$V_s = -131\ln(\text{CE}) + 2753$

Here CE stands for Cumulative Events

describe these observations. Although ‘dispersion’ is sometimes used broadly to describe frequency-dependent waveform changes, our characteristic wavelength (~ 4–5 mm) is far larger than grain size, pore scale, and fracture apertures, so the medium is effectively homogeneous at the scale of propagation and classical scattering-induced phase-velocity dispersion is unlikely. Instead, progressive damage through evolving contact stiffness, distributed microcracking, and grain crushing can increase scattering, reduce coherence, and preferentially remove higher-frequency components, producing an apparent downshift of spectral centroid/peak frequency without implying resolvable intrinsic dispersion. Therefore, our interpretation focuses primarily on how frequency-dependent scattering and energy loss reflect progressive damage mechanisms—especially as deformation transitions from brittle to cataclastic across increasing confinement. Failure at low confinement promotes brittle deformation, resulting in sharp and distinct crack planes, usually passing through the grain boundaries, with minimal grain crushing (Zhang et al. 2015). However at higher confinement, failure is accommodated by a wider, more distributed damage zone composed of many small fractures and extensive grain comminution, rather than a single sharp fracture plane, resulting in cataclastic deformation (Fig. 6) as also mentioned in Fossen et al. (2007) and Zhang et al. (2015). At the core of the failure plane, grains appear to be pulverized, representing a stark difference compared to surrounding rock mass. However, the presence of more competent and larger grains can truncate cracks (SP3-3), promoting branching of cracks to distribute accumulated stress. Such different microstructural changes affect wave propagation through the media. The contrasting spectral evolution between low and high confinement is consistent with the dominant deformation mechanism. At low confinement, failure localizes into a sharp fault plane with a comparatively narrow damage zone (Fig. 6). In this case, the fixed active-source ray path can remain largely within relatively intact material during much of loading, so the spectrum mainly shows overall attenuation rather than a systematic downshift of the dominant frequency. At higher confinement, deformation is more distributed and cataclastic (grain crushing, pore collapse, and pervasive microcracking), producing a thicker damage zone that the active wavefield must traverse. Such a distributed crack network increases scattering and reduces waveform coherence, and because higher frequencies are more sensitive to small-scale heterogeneity, the medium behaves as an effective low-pass filter, preferentially suppressing higher-frequency components and shifting the spectral peak (or centroid) toward lower frequencies (Fig. 10). Due to the directional preference of compressional and shear waves, the chance of these waves getting affected by crack formation is greater at higher confinement, as the cracks are more diffused throughout the rock mass, which also entails wave scattering. On the other hand, we have acoustic waves emitted from cracks, appearing from unknown locations in the rock mass, which therefore samples different parts of the rock mass in the ray path. Fourier transform of the active acoustic waves helps us quantify the frequency content of individual waves having the same ray path, and it is evident that the low-frequency content of the waves moves toward even lower frequency with progressive deformation at higher confinement (Fig. 10). As mentioned before, the attenuation also depends on whether the waves encounter the cracks, which has a low probability at lower confinement. This may be a possible reason why the spectral amplitudes in SP4-1 show the least change during deformation. We have excluded SP3-3 from these plots, as we do not have data to compare low-confinement and high-confinement deformation. At 3 MPa confinement, in both SP2 and 4, the peak amplitude at ~ 750 kHz shifts toward the left due to the presence of diffused cracks, whereas the low-confinement counterparts only show attenuation, but no spectral shift.

Looking at the spectral content of the AE waves (Fig. 11), a good similarity can be observed with the active acoustic waveforms (Fig. 10), where dominant frequencies can be observed around 0.75 and 1.25 MHz. For all experiments, since the onset of plasticity, more events start appearing and higher-frequency signals are more dominated in the AE waveforms, which can be attributed to propagation of crack tips as new cracks start opening up (Madariaga 1977; Li et al. 2017). Since failure at higher confinement promote generation of more shear fractures, low-frequency components naturally increase as more cracks start appearing. ####On the other hand, due to the diffused nature of crack formation, there are some higher-frequency components as well originating from newly formed crack tip (Griffith 1921). It has been experimentally shown that a slow rate of loading generally produces longer events, resulting in a lower rise angle (RA) (Naderloo et al. 2023), which is evident in our experiments (Fig. 11). For failure at low confinement, before the elastic–plastic transition, there are fewer events and they have comparatively higher average frequencies (AF) compared to the spectral content of events after the onset of plastic deformation.

A direct comparison of the active and passive observations reinforces this interpretation. The active spectra (Fig. 10) are measured along a fixed raypath and therefore isolate how evolving damage along that path reshapes the waveform; consequently, at higher confinement the preferential loss of high-frequency energy manifests as a clear downshift of the dominant peak. In contrast, AE signals (Fig. 11) originate from multiple, migrating sources and traverse variable paths through regions of variable degree of damage. This spatial averaging can reduce the visibility of a single systematic peak shift in the aggregated AE spectral metrics, even though the AE population still shows increased low-frequency contribution at higher confinement (heatmap skewness). Together, these results indicate that confinement-driven transition from brittle localization to distributed cataclastic damage produces stronger frequency-dependent attenuation in both active and passive acoustics, but it is expressed more cleanly in the controlled-path active measurements. For failure at higher confinement, insignificant changes in AF can be observed unlike the observation in active acoustic waveforms (Fig. 11). Cracks at higher confinement are more diffused and it might therefore be possible that the events originating from multiple locations average out the spectral content by sampling most of the rock mass in their ray path. Nevertheless, the heatmaps after the onset of plastic deformation show skewness toward the low-frequency domain at higher confinement, suggesting a low-frequency contribution. However, a more concrete assessment can only be provided by locating the events, which is not within the current scope of work. Isolating the spectral content of grain crushing and crack formation is challenging and has been acknowledged to be a difficult matter to deal with by previous studies (Li et al. 2017, 2023; Wang et al. 2018). Theoretical and numerical approaches have been proposed using generalized wave motion and cracking dynamics (Ono and Ohtsu 1984; Lisjak et al. 2013; Dubuc 2024); however, they are not fine-tuned for understanding rock materials. Bi et al. (2024) through extensive failure experiments on sandstones, proposed that tensile and shear events in the AF-RA space can be delineated by the following equation (Eq. 7)

$$AF = 37.41RA + 107.88. \tag{7}$$

Events above this transition line originate from tensile cracks, whereas the ones below signify shear cracking. Applying this relation, we can see that predominantly tensile

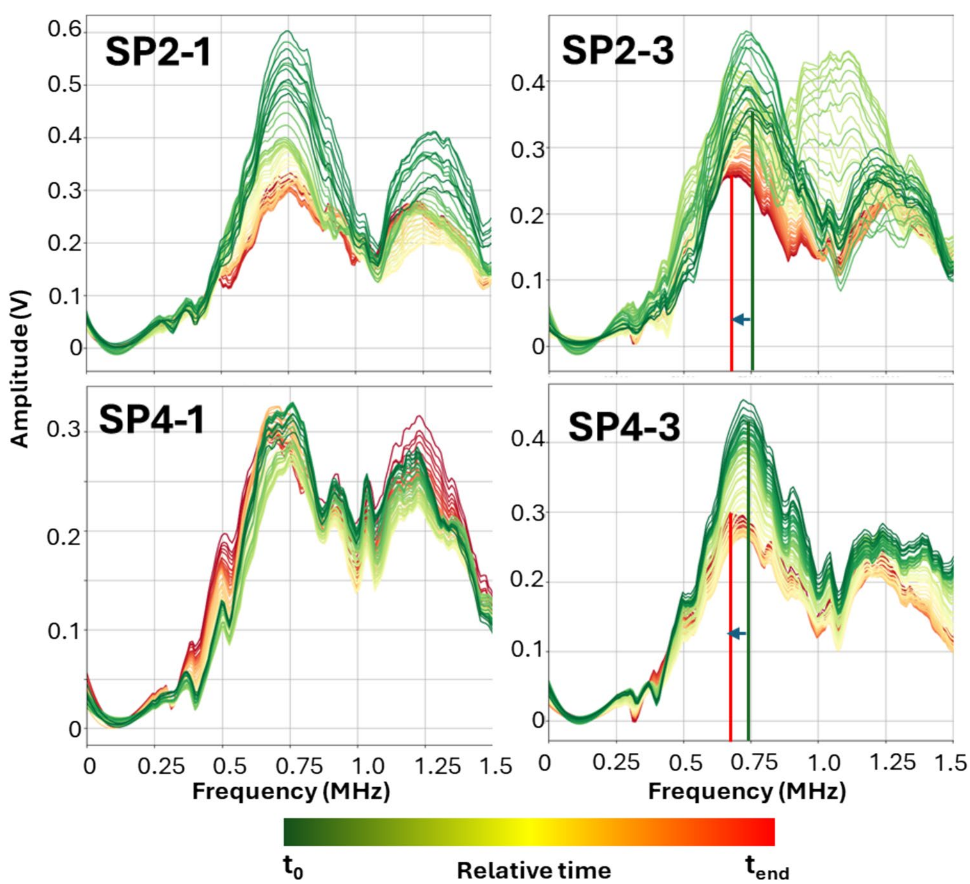

Fig. 10 Spectral content of the active acoustic waveforms recorded during the failure experiments. Dark green and red lines represent waveforms recorded at the start and end of the experiments, respectively. The dark green and red vertical lines indicate the peak amplitude and corresponding frequency of a waveform at the start and end of the experiment, respectively (Color figure online)

events appear at lower deviatoric stress, whereas more shear cracks appear since the onset of plasticity. An increase in confinement increases the proportion of shear events at both low and high deviatoric stresses. This follows the observations in previous research, which indicates that at low confinement, shear failure is a more dominant mechanism in sandstones (Kong et al. 2018; Huang et al. 2023), which is also observed in our X-ray CT images. Deformation due to stress relaxation is an extremely slow process even compared to creep and promotes aseismic crack coalescence (Zafar et al. 2022), also resulting in more tensile cracking than shear or mixed-mode cracking.

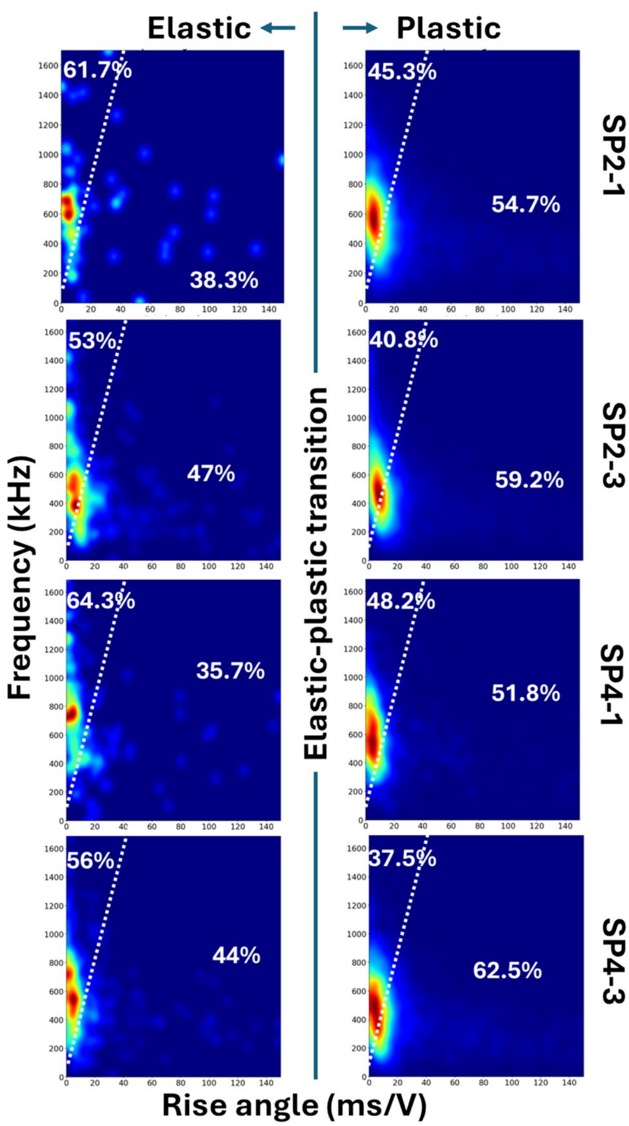

Fig. 11 Frequency versus rise angle heatmaps showing the difference of deformation mechanism before and after the onset of plasticity. The white dotted line indicates transition between tensile and shear events with the percentage contribution indicated on both sides of the line. The elastic and plastic zone of each deformation experiment is marked in Fig. 2 (Color figure online)

4.5 Relevance for Stress Monitoring and Limitations

The experiments performed in this study shed light on the relationship between deformation, sonic velocity and AE at low effective stresses for highly porous sandstones. The outcome is based on 2.6 km deep sandstones of the Aurora CO_2 storage site and are also relevant for stress monitoring during CO_2 injection in similar sites around the world. The traffic light system (Fig. 8) proposed in this study using sonic velocity and AE monitoring can help identify critical stress buildup and associated irreversible deformation in the reservoir. The correlation derived in Table 4 can help predict the number of microseismic events based on changes in Vp and Vs during irreversible deformation, which is an essential early-warning indicator for areas away from the injector which is at risk for induced seismicity. Although post-failure deformation behavior, frictional sliding, and AE are important to characterize seismic potential (Cartwright-Taylor et al. 2022), it is not the focus of this study. The effectiveness and principles of borehole sonic monitoring illustrated in this work and earlier works by Chandra and Barnhoorn (2025) and Chandra et al. (2025) will find increasing applicability with rapid implementation of downhole fiber optics for monitoring changes in acoustic properties (distributed acoustic sensing or DAS), strain (distributed strain sensing or DSS) and temperature (distributed temperature sensing or DTS) in new storage areas.

Laboratory studies related to scoping potential for CO_2 reservoirs should also include tests at or toward low-confinement pressure to better capture the non-linearity in failure criterion, inelastic strain, and failure mechanisms in reservoir sandstone. Further in situ testing in downhole condition gives us more details about the thermo-hydro-mechanical consideration in a real CO_2 injection scenario, i.e., to potentially better interpret monitoring results. The deformation mechanisms documented in this study are most relevant to localized near-wellbore regions where pore pressure increase and cooling reduce effective horizontal stress during injection. Note that the direct impact of temperature on the micromechanical processes and related effects on velocity and AE is not tested in this project and not discussed here. This is avoided due to the practical complexity of combining temperature and thermal stress paths into such experiments. However, we use the expected low effective stress induced by pore pressure and temperature changes in the field as the low effective stress boundary condition for the laboratory experiments. The results presented here are derived with a focus on the mechanical response during conventional triaxial compression stress paths, keeping isotropic stress constant and increasing the axial stress. This is also a simplification, and in the field and near-wellbore region, other stress paths are also possible, e.g., reducing effective horizontal stress and increasing effective vertical stress simultaneously.

The results are also relevant for analysis considering the area with stress redistribution and typical low effective stress very close to the borehole wall.

Under these low-confinement conditions (1 MPa), our experiments show that the transition from elastic to inelastic behavior is first expressed by a pronounced reversal in ultrasonic velocities (particularly Vs), followed by a rapid increase in AE rate. This response indicates that deformation is initially governed by localized frictional sliding and crack opening along grain boundaries, with limited grain crushing, resulting in discrete and spatially confined damage zones observed in post-deformation CT images. In contrast, experiments at 3 MPa confinement exhibit delayed velocity reversal, substantially higher cumulative AE counts, and lower peak energy per event, consistent with distributed cataclastic deformation, pore collapse, and grain crushing, evident from the post-failure 3D imaging. The temporal spreading of acoustic activity and reduced stress sensitivity at higher confinement suggest that damage accumulation is more diffused and less localized than under low-confinement conditions. These confinement-dependent differences in deformation physics imply that near-wellbore regions subjected to rapid effective stress reduction are more prone to early irreversible deformation that may not be accompanied by pronounced microseismic energy release. Consequently, the combined ultrasonic velocity–AE signatures identified in this study are particularly relevant for monitoring near-wellbore integrity during early injection and pressure transients, where localized brittle damage may precede reservoir-scale failure. In a reservoir, stress change is relatively slow compared to the laboratory scale, and the mode of deformation may vary from our observations based on the temperature, fluid composition, and rate of deformation. A better understanding through monitoring stress change signatures in reservoirs may help to ensure safe operating limit for CO_2 injection projects.

Similar to our experimental observations (Fig. 4), many studies performed at reservoir scale indicate that stress perturbation does not immediately trigger microseismicity (Walsh and Zoback 2015; Shirzaei et al. 2016; Goebel et al. 2017; Deng et al. 2020). Moreover, monitoring microseismicity alone can be misleading for high-porosity reservoir rocks, where many events are produced during elastic deformation due to grain crushing, grain sliding, clay mineral compaction (Griffiths et al. 2021), and reconfiguration of pre-existing cracks (Bernabé et al. 1994; Pijnenburg et al. 2019). The purpose of monitoring is to accurately categorize elastic and inelastic deformation behavior in reservoirs to have a better understanding of the stress state during and after injection. One way of determining the transition from elastic to plastic deformation is by assessing the increase in event rate as a function of injection rate. The traffic light system in Fig. 8 is derived from laboratory ultrasonic (MHz) velocities and acoustic emission, whereas field-scale monitoring (e.g., DAS, borehole, or surface seismic) operates at much lower frequencies (Hz–kHz) and samples a larger, heterogeneous volume. Consequently, the absolute thresholds identified here are not directly transferable. However, the underlying diagnostic sequence is scale robust. In the laboratory, the green–yellow transition is marked by a reversal or sharp reduction in the rate of change of Vs, reflecting degradation of shear stiffness and the onset of irreversible deformation; at field scale, this is expected to appear as persistent relative travel-time delays, velocity reductions, or waveform decorrelation inferred from time-lapse seismic or DAS measurements. The yellow–red transition, defined by a rapid increase in AE rate and energy, corresponds at reservoir scale to the emergence of sustained microseismic or DAS-detected event clusters. Field responses are spatially averaged and strain-rate dependent, such that localized damage may produce weaker, but more persistent precursors. Therefore, application of the traffic light framework requires reservoir-specific calibration against baseline conditions, rather than direct adoption of laboratory-derived numerical thresholds. The empirical relationships proposed in Table 4 and Fig. 9 will be essential for linking reservoir scale velocity and microseismicity measurements. Such relationship (based on reservoir specific calibration and wide array of measurements) can also help to isolate event signatures of induced seismicity and natural seismicity, avoiding false alarms in the microseismic monitoring workflow.

5 Conclusions

This study addresses the deformation behavior of highly porous sandstones from the North Sea at low confinement to highlight the deformation behavior by integrating pre- and post-deformation 3D imaging and geophysical measurement. The simultaneous use of ultrasonic wave attributes and AE measurement under controlled laboratory conditions underpins the effectiveness of such tools to accurately predict the stress state in a reservoir. This integrated monitoring approach reveals that a sudden drop in rate of change of Vp, Vs, and microseismic event rate can forecast plastic deformation in a reservoir. Such a combined monitoring approach is more effective to monitor deformation prior to yield point, where aseismic deformation may be overlooked when only microseismic monitoring is considered. Beyond the scope of CO_2 storage operation, such an approach can be applicable for monitoring any fluid injection operation in subsurface reservoirs.

Although microseismic events occur more at higher confinement (representing deeper reservoirs), the peak energy produced by an individual event is lower when compared to the peak energy produced at lower confinement. An empirical logarithmic relationship between the number of microseismic events and change in wave velocities post-yield stress has been proposed. The coefficients of this relationship also change based on confinement and can be applied to other geomaterials. While this relationship captures the coupling between damage accumulation and elastic property degradation, its quantitative form is dependent on lithology, porosity, grain size, and stress path, and therefore requires site- and reservoir-specific calibration before application at field scale.

Low-porosity and smaller-grained sandstones produce a lower number of AE events, which can be attributed to less grain crushing, emitting lower peak acoustic energies. Deformation at higher confinement also results in less peak acoustic energy. A shift toward lower frequency can be observed during deformation at higher confinement especially post-yield stress in both active acoustic and AE waveforms. This behavior can be attributed to the increasing shear cracking and grain crushing at higher confinement, also evident in the post-deformation CT images.

Comparing the experimental findings of this study and Grande et al. (2024), we can see a non-linearity in the shear failure criterion at lower confinement, which reiterates the importance of accounting for low-confinement deformation behavior when modeling CO_2 storage sites.

Supplementary Information The online version contains supplementary material available at https://doi.org/10.1007/s00603-026-05478-z.

Acknowledgements The authors acknowledge Equinor for providing samples. This publication has been produced with support from SHARP Storage (Project No. 327342). The SHARP project has been subsidized through ACT (EC Project No. 691712), by Rijksdienst voor Ondernemend Nederland (RVO). Marc Friebel and Karel Heller are duly acknowledged for their technical support in setting up the experiments. Ellen Meijvogel- de Koning is acknowledged for acquiring the CT images of the samples.

Author Contributions DC: conceptualization, methodology, experiments, writing—original draft, software, investigation, data curation. MN: writing—software, visualization, validation. LG: writing—original draft, methodology, interpretation, resources. LG: writing—review and editing, validation. AB: supervision, methodology, resources, validation, funding acquisition, project administration.

Funding Open access funding provided by NTNU Norwegian University of Science and Technology (incl St. Olavs Hospital - Trondheim University Hospital).

Data Availability Experimental data from this study are available from the corresponding author upon reasonable request.

Declarations

Conflict of Interests The authors declare no conflict of interest.

References

Amitrano D (2003) Brittle-ductile transition and associated seismicity: experimental and numerical studies and relationship with the b value. J Geophys Res Solid Earth. https://doi.org/10.1029/2001JB000680

Andfossen PO, Horntvedt L, Ravn T, et al (2012) Geological storage of CO_2 from Mongstad. Interim Report Johansen Formation. Gassnova

Agofack N, Lozovyi S, Bauer A (2018) Effect of CO_2 on P- and S-wave velocities at seismic and ultrasonic frequencies. Int J Greenh Gas Control 78:388–399. https://doi.org/10.1016/J.IJGGC.2018.09.010

Biot MA (1962) Mechanics of deformation and acoustic propagation in porous media. J Appl Phys 33:1482–1498. https://doi.org/10.1063/1.1728759

Bernabé Y, Fryer DT, Shively RM (1994) Experimental observations of the elastic and inelastic behaviour of porous sandstones. Geophys J Int 117:403–418. https://doi.org/10.1111/J.1365-246X.1994.TB03940.X

Baud P, Zhu W, Wong TF (2000) Failure mode and weakening effect of water on sandstone. J Geophys Res Solid Earth 105:16371–16389. https://doi.org/10.1029/2000JB900087

Bauer RA, Carney M, Finley RJ (2016) Overview of microseismic response to CO_2 injection into the Mt. Simon saline reservoir at the Illinois Basin-Decatur project. Int J Greenh Gas Control 54:378–388. https://doi.org/10.1016/j.ijggc.2015.12.015

Barnhoorn A, Verheij J, Frehner M et al (2018) Experimental identification of the transition from elasticity to inelasticity from ultrasonic attenuation analyses. Geophysics 83:MR221–MR229. https://doi.org/10.1190/geo2017-0534.1

Baizhanov B, Katsuki D, Tutuncu AN, Mese AI (2019) Experimental investigation of coupled geomechanical, acoustic, and permeability characterization of Berea Sandstone using a novel true triaxial assembly. Rock Mech Rock Eng 52:2491–2503. https://doi.org/10.1007/s00603-019-01816-6

Bi J, Zhao Y, Wu Z et al (2024) Research on crack classification method and failure precursor index based on RA-AF value of brittle rock. Theor Appl Fract Mech 129:104179. https://doi.org/10.1016/J.TAFMEC.2023.104179

Chandra D, Barnhoorn A (2025) Ultrasonic response of a brine-saturated reservoir rock during coupled stress and fluid perturbation during liquid-CO_2 injection. Int J Greenh Gas Control 147:104498. https://doi.org/10.1016/j.ijggc.2025.104498

Chalaturnyk R, Zambrano G, Soderberg H, et al (2006) Integrated instrumentation system in an observation well for monitoring CO_2 storage at the Penn West Pilot, Alberta, Canada. In: GHGT-8. Trondheim

Cartwright-Taylor A, Mangriotis MD, Main IG et al (2022) Seismic events miss important kinematically governed grain scale mechanisms during shear failure of porous rock. Nat Commun 13(1):13:1-14. https://doi.org/10.1038/s41467-022-33855-z

Chandra D, Alghannam L, Barnhoorn A (2025) Applicability of ultrasonic measurements to monitor and forecast stress change in subsurface storage applications. Eng Geol 359:108421. https://doi.org/10.1016/j.enggeo.2025.108421

Dubuc B (2024) Crack length directivity effects on guided-wave acoustic emission: numerical investigation of radiation patterns. Ultrasonics 137:107190. https://doi.org/10.1016/J.ULTRAS.2023.107190

Daley TM, Solbau RD, Ajo-Franklin JB, Benson SM (2007) Continuous active-source seismic monitoring of CO_2 injection in a brine aquifer. Geophysics. https://doi.org/10.1190/1.2754716

Daley TM, Myer LR, Peterson JE et al (2008) Time-lapse crosswell seismic and VSP monitoring of injected CO_2 in a brine aquifer. Environ Geol 54:1657–1665. https://doi.org/10.1007/s00254-007-0943-z

De Almeida VAD, Baptista FG, De Aguiar PR (2015) Piezoelectric transducers assessed by the pencil lead break for impedance-based structural health monitoring. IEEE Sens J 15:693–702. https://doi.org/10.1109/JSEN.2014.2352171

Deng F, Dixon TH, Xie S (2020) Surface deformation and induced seismicity due to fluid injection and oil and gas extraction in Western Texas. J Geophys Res Solid Earth 125:e2019JB018962. https://doi.org/10.1029/2019JB018962

Eiken O, Ringrose P, Hermanrud C et al (2011) Lessons learned from 14 years of CCS operations: Sleipner, In Salah and Snøhvit. Energy Proc 4:5541–5548. https://doi.org/10.1016/j.egypro.2011.02.541

Fossen H, Schultz RA, Shipton ZK, Mair K (2007) Deformation bands in sandstone: a review. J Geol Soc 164:755–769. https://doi.org/10.1144/0016-76492006-036

Fjær E, Holt RM, Horsrud P, Raaen AM (2008) Petroleum related rock mechanics. Elsevier

Fortin J, Stanchits S, Dresen G, Gueguen Y (2009) Acoustic emissions monitoring during inelastic deformation of porous sandstone: comparison of three modes of deformation. Pure Appl Geophys 166:823–841. https://doi.org/10.1007/s00024-009-0479-0

Furre A-K, Eiken O, Alnes H et al (2017) 20 years of monitoring CO_2-injection at Sleipner. Energy Proc 114:3916–3926. https://doi.org/10.1016/j.egypro.2017.03.1523

Griffith AA (1921) VI. The phenomena of rupture and flow in solids. Philos Trans R Soc Lond A Math Phys Sci 221:163–198. https://doi.org/10.1098/rsta.1921.0006

Goebel THW, Schorlemmer D, Becker TW et al (2013) Acoustic emissions document stress changes over many seismic cycles in stick-slip experiments. Geophys Res Lett 40:2049–2054. https://doi.org/10.1002/grl.50507

Goertz-Allmann BP, Kühn D, Oye V et al (2014) Combining microseismic and geomechanical observations to interpret storage integrity at the In Salah CCS site. Geophys J Int 198:447–461. https://doi.org/10.1093/GJI/GGU010

Goebel THW, Weingarten M, Chen X et al (2017) The 2016 Mw5.1 Fairview, Oklahoma earthquakes: evidence for long-range poroelastic triggering at >40 km from fluid disposal wells. Earth Planet Sci Lett 472:50–61. https://doi.org/10.1016/J.EPSL.2017.05.011

Griffiths L, Dautriat J, Vera Rodriguez I et al (2019) Inferring microseismic source mechanisms and in situ stresses during triaxial deformation of a North-Sea-analogue sandstone. Adv Geosci 49:85–93. https://doi.org/10.5194/ADGEO-49-85-2019

Griffiths L, Dautriat J, Park J, et al (2021) The influence of supercritical CO_2 saturation on the mechanical and failure properties of a North Sea reservoir Sandstone analogue. In: 15th Greenhouse gas control technologies conference 2021, GHGT 2021. https://doi.org/10.2139/SSRN.3818808

Grosse CU, Ohtsu M, Aggelis DG, Shiotani T (2022) Acoustic emission testing basics for research—applications in engineering. Springer International Publishing, Cham

Grande L, Griffiths L, Park J et al (2024) Cooling-induced geomechanical response of North Sea reservoirs, and relevance for CO_2 storage monitoring. Int J Greenh Gas Control 138:104228. https://doi.org/10.1016/J.IJGGC.2024.104228

Griffiths L, Thompson N, Smith H et al (2025) Rock mechanical testing of core from the Eos Northern Lights CCS confirmation well and implications for the geomechanics of North Sea CO_2 storage. Int J Greenh Gas Control 144:104371. https://doi.org/10.1016/J.IJGGC.2025.104371

Holloway S, Chadwick RA, Kirby GA, et al (2000) Saline Aquifer CO_2 Storage: a demonstration project at the Sleipner Field. Work area 1 (geology). https://nora.nerc.ac.uk/id/eprint/512807/1/WH00021.pdf

Hoek E, Carranza-Torres C, Corkum B (2002) Hoek-Brown failure criterion-2002 edition. In: Proceedings of NARMS-Tac. pp 267–273

Halland EK, Johansen WT, Riis F (2011) CO_2 Storage Atlas Norwegian North Sea-Norwegian Petroleum Directorate. https://www.sodir.no/490a7e/globalassets/1-sodir/publikasjoner/atlas-eng/co2-atlas-north-sea.pdf

Huang Z, Gu Q, Wu Y et al (2021) Effects of confining pressure on acoustic emission and failure characteristics of sandstone. Int J Min Sci Technol 31:963–974. https://doi.org/10.1016/J.IJMST.2021.08.003

Holt RM, Bakk A, Fjær E, et al (2023) Elastic dispersion in shale: laboratory tests and rock physics modeling. In: SEG technical program expanded abstracts 2023-August: pp 1276–1280. https://doi.org/10.1190/IMAGE2023-3910450.1

Huang J, Hua W, Li D et al (2023) Effect of confining pressure on the compression-shear fracture properties of sandstone. Theor Appl Fract Mech 124:103763. https://doi.org/10.1016/J.TAFMEC.2023.103763

Heimisson ER, Naderloo M, Chandra D, Barnhoorn A (2024) Applying and validating Coulomb rate-and-state seismicity models in acoustic emission experiments. Tectonophysics. https://doi.org/10.1016/j.tecto.2024.230574

Janssen MTG, Draganov D, Barnhoorn A, Wolf KHAA (2023) Storing CO_2 in geothermal reservoir rocks from the Kizildere field, Turkey: combined stress, temperature, and pore fluid dependence of seismic properties. Geothermics 108:102615. https://doi.org/10.1016/J.GEOTHERMICS.2022.102615

Kongsjorden H, Karstad O, Torp TA (1998) Saline aquifer storage of carbon dioxide in the Sleipner project. Waste Manag 17:303–308. https://doi.org/10.1016/S0956-053X(97)10037-X

Khazaei C, Hazzard J, Chalaturnyk R (2015) Damage quantification of intact rocks using acoustic emission energies recorded during uniaxial compression test and discrete element modeling. Comput Geotech 67:94–102. https://doi.org/10.1016/J.COMPGEO.2015.02.012

Kong R, Feng XT, Zhang X, Yang C (2018) Study on crack initiation and damage stress in sandstone under true triaxial compression. Int J Rock Mech Min Sci 106:117–123. https://doi.org/10.1016/J.IJRMMS.2018.04.019

Komijani M, Gracie R, Sarvaramini E (2019) Simulation of induced acoustic emission in fractured porous media. Eng Fract Mech 210:113–131. https://doi.org/10.1016/J.ENGFRACMECH.2018.07.028

Lüth S, Liebscher A (2017) Seismic monitoring of geological CO_2 storage. Rock Mech Eng. https://doi.org/10.1201/b20406

Lockner DA, Byerlee JD, Kuksenko V et al (1991) Quasi-static fault growth and shear fracture energy in granite. Nature 350:39–42. https://doi.org/10.1038/350039A0.

Lawton D, Couëslan M, Bland H, et al (2006) Seismic survey design for monitoring CO_2 storage: integrated multicomponent surface and borehole seismic surveys, Penn West Pilot, Alberta, Canada. In: Proceedings of the 8th international conference on greenhouse gas control technologies. pp 19–22

Lisjak A, Liu Q, Zhao Q et al (2013) Numerical simulation of acoustic emission in brittle rocks by two-dimensional finite-discrete element analysis. Geophys J Int 195:423–443. https://doi.org/10.1093/GJI/GGT221

Li C, Barès P, Laloui L (2015) A hydromechanical approach to assess CO_2 injection-induced surface uplift and caprock deflection. Geomech Energy Environ 4:51–60. https://doi.org/10.1016/J.GETE.2015.06.002

Li X, Lei X, Li Q, Li X (2017) Experimental investigation of Sinian shale rock under triaxial stress monitored by ultrasonic transmission and acoustic emission. J Nat Gas Sci Eng 43:110–123. https://doi.org/10.1016/J.JNGSE.2017.03.035

Li H, Wang F, Chen F et al (2023) Comparison of high-frequency components in acoustic emissions from rock fracture under Mode I and Mode II dominated loading. Int J Rock Mech Min Sci 170:105554. https://doi.org/10.1016/J.IJRMMS.2023.105554

Lozovyi S, Duda M, Bauer A, Holt RM (2024) Stress path dependence of time-lapse seismic effects in shales: experimental comparison at seismic and ultrasonic frequencies. Geophys J Int 240:446–461. https://doi.org/10.1093/GJI/GGAE290

Madariaga R (1977) High-frequency radiation from crack (stress drop) models of earthquake faulting. Geophys J Int 51:625–651. https://doi.org/10.1111/J.1365-246X.1977.TB04211.X

Mathieson A, Midgely J, Wright I et al (2011) In Salah CO_2 storage JIP: CO_2 sequestration monitoring and verification technologies applied at Krechba, Algeria. Energy Proc 4:3596–3603. https://doi.org/10.1016/J.EGYPRO.2011.02.289

Mayr SI, Stanchits S, Langenbruch C et al (2011) Acoustic emission induced by pore-pressure changes in sandstone samples. Geophysics. https://doi.org/10.1190/1.3569579

Meneguolo R, Målbakken T, Galvani L, et al (2020) Subsurface contributions to the Northern Lights CO_2 storage project sanction: planning for success in an unexplored license. In: Proceedings of the SPE Aberdeen carbon capture utilisation and storage conference. Aberdeen

Meneguolo R, Sundal A, Martinius AW et al (2022) Impact of the lower Jurassic Dunlin Group depositional elements on the Aurora CO2 storage site, EL001, northern North Sea, Norway. Int J Greenh Gas Control 119:103723. https://doi.org/10.1016/J.IJGGC.2022.103723

McBeck J, Cordonnier B, Zhu W, Renard F (2026) Transition from fracture propagation to coalescence in Westerly Granite during the preparation process of macroscopic failure. J Geophys Res Solid Earth 131:e2025JB032676. https://doi.org/10.1029/2025JB032676

Northern Lights JV (2023) Rock mechanics data for 31/5-7 Eos well core—datasets—CO_2 DataShare. https://co2datashare.org/dataset/rock-mechanics-data-for-31-5-7-eos-well-core

Naderloo M, Veltmeijer A, Jansen JD, Barnhoorn A (2023) Laboratory study on the effect of stress cycling pattern and rate on seismicity evolution. Geomech Geophys Geo-Energy Geo-Res 9:1–18. https://doi.org/10.1007/s40948-023-00678-1

O'Connell RJ, Budiansky B (1974) Seismic velocities in dry and saturated cracked solids. J Geophys Res 79:5412–5426. https://doi.org/10.1029/JB079i035p05412

Ono K, Ohtsu M (1984) A generalized theory of acoustic emission and Green's functions in a half space. J Acoust Emiss 3:27–40

Pijnenburg RPJ, Verberne BA, Hangx SJT, Spiers CJ (2019) Inelastic deformation of the Slochteren Sandstone: stress-strain relations and implications for induced seismicity in the Groningen gas field. J Geophys Res Solid Earth 124:5254–5282. https://doi.org/10.1029/2019JB017366

Pevzner R, Isaenkov R, Yavuz S et al (2021) Seismic monitoring of a small CO_2 injection using a multi-well DAS array: operations and initial results of stage 3 of the CO2CRC Otway project. Int J Greenh Gas Control 110:103437. https://doi.org/10.1016/j.ijggc.2021.103437

Rutqvist J, Vasco DW, Myer L (2010) Coupled reservoir-geomechanical analysis of CO_2 injection and ground deformations at In Salah, Algeria. Int J Greenh Gas Control 4:225–230. https://doi.org/10.1016/J.IJGGC.2009.10.017

Ringrose PS, Mathieson AS, Wright IW et al (2013) The In Salah CO_2 storage project: lessons learned and knowledge transfer. Energy Proc 37:6226–6236. https://doi.org/10.1016/J.EGYPRO.2013.06.551

K RK, H H, D C et al (2023) Comprehensive review of geomechanics of underground hydrogen storage in depleted reservoirs and salt caverns. J Energy Storage 73:108912. https://doi.org/10.1016/J.EST.2023.108912

Scholz CH (1968) The frequency-magnitude relation of microfracturing in rock and its relation to earthquakes. Bull Seismol Soc Am 58:399–415. https://doi.org/10.1785/BSSA0580010399

Siggins AF, Dewhurst DN (2003) Saturation, pore pressure and effective stress from sandstone acoustic properties. Geophys Res Lett. https://doi.org/10.1029/2002GL016143

Sellers EJ, Kataka MO, Linzer LM (2003) Source parameters of acoustic emission events and scaling with mining-induced seismicity. J Geophys Res Solid Earth 108:2418. https://doi.org/10.1029/2001JB000670

Shirzaei M, Ellsworth WL, Tiampo KF et al (2016) Surface uplift and time-dependent seismic hazard due to fluid injection in eastern Texas. Science 353:1416–1419. https://doi.org/10.1126/science.aag0262

Smeraglia L, Bettucci A, Billi A et al (2017) Microstructural evidence for seismic and aseismic slips along clay-bearing, carbonate faults. J Geophys Res Solid Earth 122:3895–3915. https://doi.org/10.1002/2017JB014042

Sang G, Liu S, Elsworth D (2020) Quantifying fatigue-damage and failure-precursors using ultrasonic coda wave interferometry. Int J Rock Mech Min Sci 131:104366. https://doi.org/10.1016/J.IJRMMS.2020.104366

Vavryčuk V (2001) Inversion for parameters of tensile earthquakes. J Geophys Res Solid Earth 106:16339–16355. https://doi.org/10.1029/2001JB000372.

Teatini P, Gambolati G, Ferronato M et al (2011) Land uplift due to subsurface fluid injection. J Geodyn 51:1–16. https://doi.org/10.1016/J.JOG.2010.06.001

Thompson N, Andrews JS, Bjørnarå TI (2021) Assessing potential thermo-mechanical impacts on caprock due to CO_2 injection—a case study from Northern Lights CCS. Energies 14:5054–5054. https://doi.org/10.3390/EN14165054

Thompson N, Andrews JS, Wu L, Meneguolo R (2022) Characterization of the in-situ stress on the Horda platform—a study from the Northern Lights Eos well. Int J Greenh Gas Control 114:103580. https://doi.org/10.1016/J.IJGGC.2022.103580

Veltmeijer A, Naderloo M, Barnhoorn A (2023) Active and passive seismic monitoring of laboratory-based injection-driven fault reactivation. In: 84th EAGE annual conference and exhibition, vol 1. pp 317–321. https://doi.org/10.3997/2214-4609.202310513

Thompson N, Griffiths L, Bjørnarå TI, et al (2024) Experimental and numerical validation of cooling-induced stress change within a caprock shale—seal integrity insights from the northern lights CCS project. In: 58th US rock mechanics/geomechanics symposium. https://doi.org/10.56952/ARMA-2024-0089

Veltmeijer A, Naderloo M, Barnhoorn A (2024) Precursors to rock failure in the laboratory using ultrasonic monitoring methods. Geomech Geophys Geo-Energy Geo-Resour 10:1–15. https://doi.org/10.1007/s40948-024-00812-7

Walsh JB (1965) The effect of cracks on the uniaxial elastic compression of rocks. J Geophys Res 70:399–411. https://doi.org/10.1029/JZ070i002p00399

Walsh FR, Zoback MD (2015) Oklahoma's recent earthquakes and saltwater disposal. Sci Adv. https://doi.org/10.1126/sciadv.1500195

Wong T, David C, Zhu W (1997) The transition from brittle faulting to cataclastic flow in porous sandstones: mechanical deformation. J Geophys Res Solid Earth 102:3009–3025. https://doi.org/10.1029/96JB03281

Will R, Smith V, Leetaru HE et al (2014) Microseismic monitoring, event occurrence, and the relationship to subsurface geology. Energy Proc 63:4424–4436. https://doi.org/10.1016/J.EGYPRO.2014.11.478

Wang X, Wu S, Ge H et al (2018) The complexity of the fracture network in failure rock under cyclic loading and its characteristics in acoustic emission monitoring. J Geophys Eng 15:2091–2103. https://doi.org/10.1088/1742-2140/AABF1C

White D, Daley TM, Paulsson B, Harbert W (2021) Borehole seismic methods for geologic CO_2 storage monitoring. Lead Edge 40(6):434–441. https://doi.org/10.1190/TLE40060434.1

Yang SQ, Huang YH, Ranjith PG (2018) Failure mechanical and acoustic behavior of brine saturated-sandstone containing two pre-existing flaws under different confining pressures. Eng Fract Mech 193:108–121. https://doi.org/10.1016/J.ENGFRACMECH.2018.02.021

Yang SQ, Huang YH, Tang JZ (2020) Mechanical, acoustic, and fracture behaviors of yellow sandstone specimens under triaxial monotonic and cyclic loading. Int J Rock Mech Min Sci 130:104268. https://doi.org/10.1016/J.IJRMMS.2020.104268

Zafar S, Hedayat A, Moradian O (2022) Micromechanics of fracture propagation during multistage stress relaxation and creep in brittle rocks. Rock Mech Rock Eng 55:7611–7627. https://doi.org/10.1007/s00603-022-03045-w

Zhang Y, Shao JF, Xu WY et al (2015) Experimental and numerical investigations on strength and deformation behavior of cataclastic sandstone. Rock Mech Rock Eng 48:1083–1096. https://doi.org/10.1007/s00603-014-0623-8

Zotz-Wilson R, Boerrigter T, Barnhoorn A (2019) Coda-wave monitoring of continuously evolving material properties and the precursory detection of yielding. J Acoust Soc Am 145:1060–1068. https://doi.org/10.1121/1.5091012

Zhao K, Yang D, Zeng P et al (2021) Accelerating creep stage of red sandstone expressed and quantitatively identified based on acoustic emission information. Rock Mech Rock Eng 54:4867–4888. https://doi.org/10.1007/s00603-021-02529-5